

1 **In-situ Rb-Sr geochronology of white mica in young metamafic and**  
2 **metasomatic rocks from Syros: testing the limits of LA-ICP-MS/MS mica**  
3 **dating using different anchoring approaches**

4 Jesús Muñoz-Montecinos <sup>1</sup>, Andrea Giuliani <sup>2,3</sup>, Senan Oesch<sup>2</sup>, Silvia Volante <sup>1</sup>, Bradley  
5 Peters<sup>2</sup>, Whitney Behr <sup>1</sup>

6  
7 <sup>1</sup> Institute of Geology, Department of Earth Sciences, ETH Zurich

8 <sup>2</sup> Institute of Geochemistry and Petrology, Department of Earth Sciences, ETH Zurich

9 <sup>3</sup> Earth and Planets Laboratory, Carnegie Institution for Science

10  
11 \* Correspondence to: Jesús Muñoz-Montecinos (jmunoz@ethz.ch)

12  
13 **Abstract**

14 The recent development of LA-ICP-MS/MS has revolutionized Rb-Sr mica dating allowing to  
15 obtain isotopic data within their microstructural context. While effective for old and felsic  
16 materials, this method presents challenges for young metamafic and metasomatic rocks due to  
17 limited radiogenic ingrowth associated with low Rb/Sr and young ages. We quantitatively  
18 address these limitations by combining laser ablation ICP-MS/MS and MC-ICP-MS data for  
19 coexisting white mica and epidote, respectively, for 10 Cenozoic metamorphic rocks from  
20 Syros Island (Greece). White mica analyses from metamafic and metasomatic rocks yield  
21 limited Rb/Sr spread, which typically does not exceed one order of magnitude ( $^{87}\text{Rb}/^{86}\text{Sr} = 14$   
22 to 231 for the combined dataset), and low radiogenic  $^{87}\text{Sr}/^{86}\text{Sr}$  (generally  $<0.8$ ), resulting in  
23 high age uncertainties of typically 10 to 50% relative standard error (RSE), and thus hampering  
24 robust geological interpretations. Epidote  $^{87}\text{Sr}/^{86}\text{Sr}$  values range between  $\sim 0.705$  and  $0.708$ .  
25 The former is typically expected for unaltered metamafic materials, whereas the latter is  
26 interpreted to reflect fluid-rock interaction along shear zones, with fluids derived from or  
27 having interacted with more radiogenic lithologies. These atypical values suggest that a  
28 commonly assumed value of  $0.703$  for mafic rocks may not always be representative.  
29 Anchoring white mica Rb-Sr to epidote  $^{87}\text{Sr}/^{86}\text{Sr}$  data improves age accuracy and precision  
30 substantially (e.g.,  $29 \pm 17$  Ma vs  $47.2 \pm 4.4$  Ma for sample SYGR36). The new ages obtained  
31 in this study are consistent with multiple events previously recorded in Syros and the Cyclades  
32 blueschists unit including: i) metasomatism and metamorphism at near-peak to epidote  
33 blueschist-facies conditions during early exhumation (c. 47 Ma to 41 Ma); and ii) a late stage  
34 of high-pressure exhumation and metasomatism transitioning to blueschist-greenschist facies  
35 conditions (c. 21 Ma to 20 Ma). Anchored white-mica Rb-Sr ages in mafic rocks allow us to  
36 discriminate events of fluid-rock interactions and metasomatism associated with shear zone  
37 deformation at the subduction interface.

38  
39 **Keywords**

40 Rb-Sr dating; White mica; epidote; Syros; Metamorphism; Metasomatism

## 43 Introduction

44 Subduction zones host a wide range of mechanical and chemical processes that occur at various  
45 spatial and temporal scales including seismicity, element transfer, volcanism and orogenesis  
46 (e.g., Breeding et al., 2004; Burg and Bouilhol, 2019; Muñoz-Montecinos et al., 2021; Li et al.  
47 2021; Wirth et al., 2022; Tumiati et al., 2022; Bastias et al., 2023; Rubatto et al., 2023). These  
48 processes are temporally associated with metamorphism, fluid-rock interactions and  
49 metasomatism at depth and occur over time-scales ranging from those of steady-state tectonics  
50 (e.g., nappe stacking over millions of years; Rubatto et al., 2011; Holtmann et al., 2022) to  
51 nearly instantaneous mineral growth and fluid flow (John et al., 2012). Constraining the timing  
52 of high-pressure and low-temperature (HP-LT) mineral growth and fabric development is  
53 therefore crucial for understanding deep tectono-thermal processes. However, accurately  
54 dating these subduction-related metamorphic events remains challenging.

55  
56 Compared to felsic rocks, dating metamafic rocks is challenging due to the paucity of minerals  
57 amenable to geochronology. While the U-Pb system has been employed to date HP-LT mafic  
58 metamorphic rocks, it relies on the presence of U-bearing accessory phases such as zircon,  
59 allanite, titanite, rutile, and apatite which may be scarce, too small to be targeted, or have low-  
60 U concentrations (e.g., Timmermann et al., 2004; Rubatto et al., 2011; Regis et al., 2014; Engi  
61 et al. 2017; Holtmann et al., 2022; Volante et al. 2024 and references therein). Additionally, it  
62 is challenging to link microstructures with U-Pb dates of accessory minerals due to their often-  
63 ambiguous textural association with the microfabrics. Therefore, alternative minerals and  
64 systematics are essential for a comprehensive record of deformation and metamorphism in HP  
65 metamafic rocks.

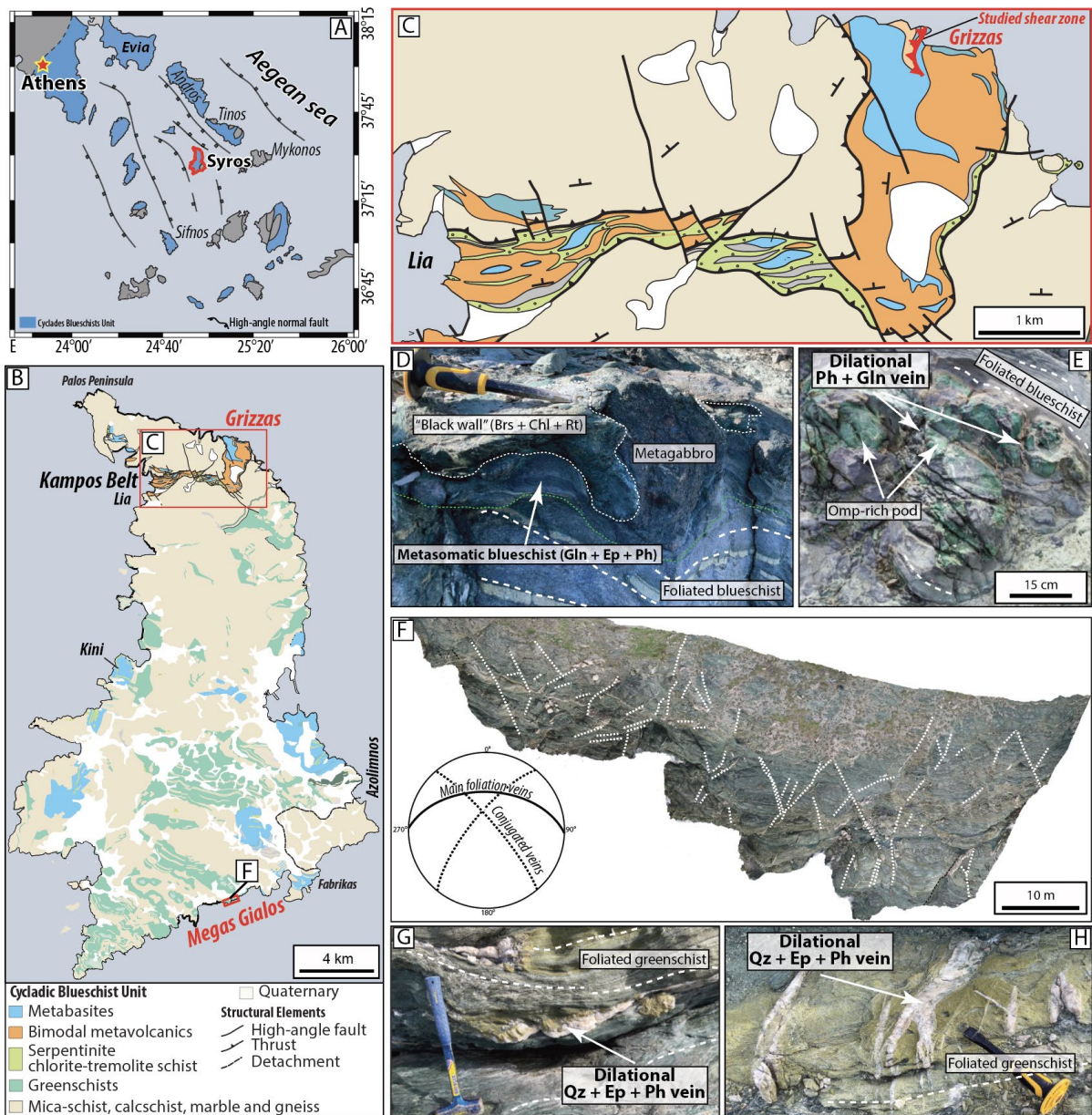
66  
67 White mica is a common mineral in HP-LT altered oceanic metamafic and metasedimentary  
68 lithologies and is stable throughout prograde and retrograde reactions (Schmidt et al., 2004;  
69 Halama et al., 2020). The high Rb contents and the estimated high closure temperature of the  
70 Rb-Sr system in this mineral ( $500 \pm 50$  °C – Jäger et al., 1967; von Blanckenburg et al, 1989;  
71 Villa, 1998; Glodny et al. 1998, 2008) make white mica a suitable geochronometer for dating  
72 subduction-related processes, especially when combined with low Rb/Sr phases. Despite the  
73 robustness of multimineral Rb-Sr isochron analyses (Glodny et al., 2004, 2008; Wawrzenitz et  
74 al., 2006; Bröcker et al., 2013; Kirchner et al., 2016; Angiboust and Glodny, 2020), significant  
75 challenges remain. These include: i) Sr isotope disequilibrium between micas and the other  
76 mineral phases; ii) coexistence of several generations of micas; iii) post-deformation, low-  
77 temperature magmatic alteration or fluid-assisted recrystallization; iv) thermally-induced  
78 diffusion processes (Glodny and Ring 2022); and v) potential inheritance within mica grains  
79 or across mica populations (Villa, 2016; Barnes et al., 2024). These variations in mica Rb-Sr  
80 systematics and isotopic variability can be directly addressed using in-situ laser ablation  
81 methods (e.g., Ribeiro et al., 2023a).

82  
83 In-situ Rb-Sr dating of white mica using a laser-ablation triple-quadrupole inductively coupled  
84 plasma mass spectrometer (LA-ICP-MS/MS) offers significant advantages over conventional

85 ID (isotope dilution) TIMS analyses. This technique eliminates the need for mineral separation  
86 and time-consuming chromatographic column chemistry, enabling quick, cost-effective  
87 analyses. It further allows to constrain potential zoning in Rb-Sr isotope distribution  
88 (Kutzschbach and Glodny, 2024; Rösel and Zack, 2021), hence preserving essential textural  
89 information which is otherwise lost. Thus, potential age variations among different white mica  
90 populations (e.g., syn- to post-kinematic grains) within distinct microstructural domains such  
91 as microfolds, shear zones, and boudin necks permit a more accurate interpretation of the  
92 resulting ages (Gou et al., 2022; Gyomlai et al., 2022, 2023a; Kirkland et al., 2023; Ribeiro et  
93 al., 2023b; Ceccato et al., 2024; Barnes et al., 2024). This method has been extensively applied  
94 to constrain the timing of deformation events in Precambrian-Paleozoic felsic lithologies  
95 (Olierook et al., 2020; Tillberg et al., 2021; Wang et al., 2022; Ribeiro et al., 2023b), but its  
96 application remains limited in mafic lithologies. For example, a recent study on mafic  
97 blueschist from the Syros island (Greece) presented white mica-only isochron ages interpreted  
98 to date fluid-rock interactions along the subduction interface (Gyomlai et al., 2023a). More  
99 accurate age constraints were obtained by combining Rb-Sr dating of white mica with initial  
100 Sr isotope constraints of epidote and apatite in metamafic rocks from Syros (Barnes et al.,  
101 2024).

102  
103 These studies highlight the great potential of in-situ mica Rb-Sr geochronology by LA-ICP-  
104 MS/MS to investigate different rock-types and geological questions (e.g., Redaa et al., 2022;  
105 Wang et al., 2022; Zametzer et al., 2022; Huang et al., 2023; Giuliani et al., 2024). Yet, it  
106 remains challenging to date young (i.e., Cenozoic) metamafic and metasomatic lithologies with  
107 low Rb contents (e.g., <30 ppm in mafic rocks) and associated low Rb/Sr micas where ingrowth  
108 of radiogenic Sr is limited. In this contribution, we address the limitations of in-situ Rb-Sr  
109 dating of white mica in young metamafic and metasomatic rocks and propose strategies to  
110 obtain robust Rb-Sr ages using laser ablation methods. We present new data of 10 samples  
111 from Syros Island (Kampos Belt and Megas Gialos area; Greece) and integrate petrographic  
112 and textural analysis of HP-LT rocks with laser ablation Rb-Sr analyses of white mica and  
113 multi-collector (MC) ICP-MS Sr isotope analyses of epidote (complemented with bulk rock Sr  
114 isotopes for some of the samples). Although the general architecture and structural  
115 relationships of blueschist- to eclogite-facies rocks in Syros are still debated (e.g., Keiter et al.,  
116 2011; Laurent et al., 2018; Kotowski et al., 2022), the subdivision of geological units, P-T  
117 conditions and the timing of metamorphic burial and exhumation are well-constrained, making  
118 Syros an ideal case study for our purpose. We demonstrate that in these young (Cenozoic)  
119 metasomatic and metamafic rocks, anchoring mica-based Rb-Sr isochrons to initial (or  
120 ‘common’)  $^{87}\text{Sr}/^{86}\text{Sr}$  from a cogenetic phase such as epidote or a geologically meaningful  
121 ‘model’ (e.g., Rosel and Zack, 2021) circumvent issues with low Rb-Sr ratios in these rocks.

122  
123  
124



125  
 126 **Figure 1.** A. Simplified geologic map of the Cyclades highlighting the location of Syros Island. B. Simplified  
 127 geologic map of Syros Island (modified from Keiter et al., 2011); the study localities are highlighted in red. C.  
 128 Zoom in of the Kampos Belt; the study locality is shown in red. D. Field image of an omphacitite pod embedded  
 129 in a foliated blueschist matrix within the Grizzas shear zone, the former contains some of the studied glaucophane  
 130 + phengite dilational veins (sample SYGR41). E. Representative field image of metasomatic rocks from the  
 131 Grizzas shear zone; note the occurrence of smeared metagabbro blocks surrounded by metasomatic rinds and  
 132 black walls within a foliated blueschist and a chlorite-tremolite schists matrix. F. Orthomosaic image from the  
 133 Megas Gialos outcrop (inset from panel B; modified from Muñoz-Montecinos and Behr, 2023). The lower-  
 134 hemisphere stereonet depicts the orientation of the veins following the main foliation as well as those sets oblique  
 135 to it (dashed white lines illustrate the orientation of conjugated vein sets), represented here by samples SYMG08.3  
 136 and SYMG02, respectively. G and H. Examples of dilational veins containing epidote fibers along with phengite.

## 137 Geological setting

### 138 Syros Island

139 The HP-LT rocks from Syros Island belong to the Cyclades Blueschists Unit (CBU) cropping  
140 out along the Aegean Sea (**Figure 1A and 1B**). The CBU is interpreted to represent exhumed  
141 fragments of the subducted Adriatic plate and HP-LT meta-ophiolites of a northward-dipping  
142 subduction event between the Eurasian and African plates (Gautier and Brun, 1994; Jolivet et  
143 al., 2010; Soukis and Stockli, 2012). The CBU is subdivided into three subgroups (Glodny and  
144 Ring, 2022), from which the Top and Middle CBU nappes are relevant for this study. The Top  
145 CBU nappe crops out in Syros as a narrow belt, known in the literature as the Kampos Belt, to  
146 which one of the study localities belong to: the Grizzas shear zone (**Figure 1C**). It is composed  
147 of abundant metavolcanic materials with a bimodal composition (mafic and felsic) along with  
148 metagabbros, serpentinites, tremolite-chlorite, talc- and garnet schists (Keiter et al., 2011). The  
149 Kampos Belt lithologies reached peak blueschist- to eclogite-facies conditions of 480–560°C  
150 and 1.6–2.2 GPa (e.g., Trotet et al., 2001; Laurent et al., 2018; Cisneros et al., 2020). The  
151 Middle CBU nappe is the most abundant unit and is mainly composed of a relatively coherent  
152 intercalation of marbles, metasediments and metabasites (**Figure 1B**). This latter lithotype  
153 represents the studied lithology at the Megas Gialos locality (**Figure 1B and 1F**), displaying a  
154 pervasive exhumation overprint transitioning from blueschist- to greenschist-facies from 450  
155 to 400 °C and 1.4 to 1.0 GPa (Cisneros et al., 2020). These retrograde metamorphic conditions  
156 are associated with transient brittle fracturing and dilational veining (Muñoz-Montecinos and  
157 Behr, 2023), from which the investigated samples from Megas Gialos were collected.

158 The pre-subduction architecture of the CBU resulted from Triassic rifting of the basement  
159 accompanied by deposition of passive margin sediments and carbonates (Keay, 1998; Seman  
160 et al., 2017). Rifting occurred at c. 80 Ma, thinning the lithosphere and producing small-scale  
161 oceanic basins along with passive margin depocenters (Keiter et al., 2011; Cooperdock et al.,  
162 2018; Kotowski et al., 2022). In the Kampos Belt (Grizzas locality), U-Th-Pb SHRIMP zircon  
163 analyses in a metagabbro and a meta-plagiogranitic dike reveal two age populations, one at c.  
164 80 Ma and a second one at  $52.4 \pm 0.8$  Ma (Tomaschek et al., 2003). The older age likely reflects  
165 the magmatic crystallization, whereas the younger one dates the HP-LT peak metamorphism.  
166 Phengite and multi-mineral Rb-Sr (e.g., white mica + epidote + glaucophane +/- omphacite +/-  
167 garnet), phengite Ar-Ar and garnet Lu-Hf ages (mostly from the Lia side, hereafter referred to  
168 as the Western Kampos Belt) are in the range of 55 to 44 Ma, and were interpreted to reflect  
169 the timing of prograde-to-peak HP-LT metamorphism (see Kotowski et al., 2022 and  
170 references therein). Similar peak ages of  $51.8 \pm 0.1$  Ma were obtained by Lu-Hf geochronology  
171 of garnet in a metasedimentary rock from the Fabrikas outcrop in south Syros Island (Tual et  
172 al., 2022). The initial stage of exhumation under blueschist-facies conditions likely began at c.  
173 44 Ma and transitioned to greenschist-facies conditions between 34 and 20 Ma based on Ar-Ar  
174 and Rb-Sr multi-mineral (e.g., white mica + epidote + albite) geochronology (e.g. Putlitz et al.,  
175 2005; Uunk et al., 2018; Glodny and Ring, 2022 and references therein). Gyomlai et al. (2023a)

176 obtained three in-situ mica Rb-Sr ages from an outcrop within the Kampos belt (Lia side) in  
177 the range of  $36.3 \pm 5.1$  Ma to  $36.1 \pm 4.7$  Ma, inferred to date metasomatism of metamafic rocks  
178 during blueschist- to greenschist-facies exhumation. The authors also reported older ages in the  
179 range of  $52.5 \pm 11.6$  to  $39.8 \pm 7.4$  Ma (Kampos belt, Lia side), but it is unclear whether these  
180 ages represent metasomatism and/or mineral (re)crystallization during peak metamorphism or  
181 retrogression during HP to late exhumation. Multi-mineral and in-situ white mica Rb-Sr and  
182 Ar-Ar dating in the Middle CBU nappe yielded peak HP-LT metamorphism ages of 45 to 37  
183 Ma, whereas the pervasive blueschist- to greenschist-facies metamorphism is dated at c. 39 to  
184 19 Ma (Glodny and Ring 2022; Barnes et al., 2024; Kotowski et al., 2022 and references  
185 therein).

## 186 **Samples and Petrography**

187 In this section, we present key petrographic observations of the 10 samples from the Syros  
188 Island that have been selected for Rb-Sr dating (**Table 1**), emphasizing the textural context of  
189 white mica and epidote. Two additional samples (SYGR50 and SYGR44) have been analyzed  
190 for epidote  $^{87}\text{Sr}/^{86}\text{Sr}$  only. The investigated samples were carefully selected in order to  
191 constrain the timing of fluid-rock interaction (metasomatism and veining) and to evaluate the  
192 significance of  $^{87}\text{Sr}/^{86}\text{Sr}$  isotopic values for anchoring white mica Rb-Sr isochrons. We targeted  
193 our samples based on the presence of white mica in apparent textural equilibrium with epidote  
194 (where present) and, for the Grizzas samples, the apparent absence of greenschist-facies  
195 overprinting.

196  
197 The samples coded SYGR (seven out of nine samples were dated) all belong to the Grizzas  
198 locality in the easternmost part of the Kampos Belt (**Figure 1B and 1C**). These samples were  
199 collected along a north-dipping shear zone (hereafter referred to as the Grizzas shear zone),  
200 which juxtaposes a massive to variably strained metagabbro and blueschist-facies igneous  
201 breccia, representing a region of high and localized strain (**Figure 1C**; see also Keiter et al.,  
202 2011). Samples SYGR36 and SYGR44 correspond to relict (partially digested) blueschist  
203 blocks, while sample SYGR50 represents a pristine, low-strain metagabbro. SYGR37 and  
204 SYGR38 represent the metasomatized mafic matrix wrapping around the metagabbro and  
205 blueschist blocks (i.e., metasomatic rinds in **Figure 1D**), whereas sample SYGR42 is an altered  
206 metagabbro (see **Table 1** for a summary of the studied samples). For comparison, a  
207 metasedimentary rock sample (SYGR45) from a  $\sim 70$  cm thick discrete layer within the shear  
208 zone as well as a felsic pod (sample SYGR58) contained within a moderately-strained meta-  
209 igneous breccia (e.g., Keiter et al., 2011), were also targeted for dating. We emphasize the  
210 occurrence of dilational phengite + glaucophane veins (such as sample SYGR41) cross-cutting  
211 omphacite pods (**Figure 1E**). The samples coded SYMG were collected from a retrograde  
212 greenschist-to-blueschist-facies sliver located in the Megas Gialos locality (**Figure 1F**). The  
213 selected vein samples SYMG02 and SYMG08.3 (**Figure 1G and 1H**) formed as dilational  
214 fractures related to the ascent of deep subduction zone fluids towards the base of the fore arc  
215 during the latest stages of HP-LT exhumation and extension (e.g., Muñoz-Montecinos and

216 Behr, 2023). Sample SYMG07 represents the greenschist host rock associated with the vein  
 217 samples SYMG02 and SYMG08.3

**Table 1. Sample summary**

Sample ID	Rock type and general structure	Mineral assemblage	Analysed microdomain
<i>Grizzas shear zone (NE Syros)</i>			
<i>Blueschist-facies</i>			
SYGR36	Strongly foliated blueschist block	Gln + Ep + Wm + Gte + Omp + Rt	Wm defining the main foliation and pressure shadows around Gte
SYGR37	Moderate to strongly foliated metasomatic rind	Gln + Ep + Wm + Chl	Wm defining the main foliation
SYGR38	Weakly foliated metasomatic rind	Gln + Ep + Wm + Chl	Randomly oriented and interlocked Wm and Ep
SYGR41	Dilational vein	Gln + Wm	Randomly oriented laths of Wm
SYGR42	Moderately foliated metagabbro	Gln + Wnc + Omp + Ep + Wm + Rt	Shear bands defining the main foliation
SYGR44	Moderately foliated blueschist block	Gln + Lws (now Ep + Wm) + Wm + Gte + Rt	Ep replacing Lws pseudomorphs
SYGR45	Foliated metasediment	Wm + Gln + Gte + Ep + Tur	Wm aligned and oblique according to the main foliation
SYGR50	Weakly to moderately foliated metagabbro	Omp + Ep + Gln + Wm	Ep defining the main foliation and within boudin necks
SYGR58	Moderately foliated felsic pod	Qz + Wm	Wm aligned and oblique according to the main foliation
<i>Megas Gialos (SE Syros)</i>			
<i>(HP)Greenschist-facies</i>			
SYMG02	Dilational vein	Qz + Ep + Wm + Ab	Ep fibers and Wm laths in close contact
SYMG07	Moderately to strongly foliated	Ep + Ab + Chl + Act + Wm + Ttn	Ep and Wm defining the main foliation
SYMG08.3	Dilational vein	Qz + Ep + Wm	Ep fibers and Wm laths in close contact

218  
 219 *Table 1. Summary of the samples selected for this study as well as their corresponding rock type, mineral*  
 220 *assemblage (major minerals) and analyzed microdomains. Mineral abbreviations are from Whitney and Evans*  
 221 *(2010). Chl – chlorite; Ep – epidote; Gln – glaucophane; Grt – garnet; Omp – omphacite; Qz – quartz; Ttn –*  
 222 *titanite; Tur – tourmaline; Wm – white mica; Wnc – winchite.*

## 223 **Blueschists, blueschist-facies metagabbro and greenschist**

224 Samples SYGR36 and SYGR44 are relict blueschist blocks within a metasomatized sheared  
 225 matrix. Glaucophane, together with white mica and epidote define the penetrative foliation.  
 226 Texturally, white mica occurs as medium-grained laths and displays no evidence of kinks,  
 227 undulose extinction or fish. In sample SYGR36, white mica also occurs within pressure  
 228 shadows (**Figure 2A**) and boudin necks around garnet as well as oblique to the main foliation.  
 229 No significant zoning patterns in major elements were observed (**Supplementary Figure S1A-**  
 230 **F**; see also **Figure S2** for white mica mineral chemistry data). Mostly, white mica grains  
 231 defining the main foliation as well as those spatially related to pressure shadows were targeted  
 232 for dating. Sample SYGR44 texturally preserves lozenge-shaped lawsonite pseudomorphs now  
 233 composed of strain-free epidote (targeted for  $^{87}\text{Sr}/^{86}\text{Sr}$  analyses) and white mica  
 234 (**Supplementary Figure S1G**).

235

236 Sample SYGR50 is a low-strain metagabbro composed of coarse-grained clinopyroxene  
237 pseudomorphs (now glaucophane, winchite and omphacite) in a matrix of epidote. The (weak)  
238 foliation is defined by elongated tabular crystals of epidote and subordinate white mica. Boudin  
239 necks within large porphyroclasts are filled by epidote, white mica and garnet (**Supplementary**  
240 **Figure S1H**). In this sample, epidote crystals defining the foliation and filling the boudin necks  
241 were targeted for  $^{87}\text{Sr}/^{86}\text{Sr}$  analyses. Overall, this sample represents the weakly-metasomatized  
242 analogue of the altered metagabbro sample SYGR42.

243

244 Sample SYMG07 is a coarse-grained greenschist and represents the host rock associated with  
245 the vein samples SYMG02 and SYMG08.3. The main foliation is defined by amphibole and  
246 epidote, oriented laths of chlorite and white mica as well as stretched albite (**Figure 2B**).  
247 Phengite grains in the matrix exhibit weak core-mantle zoning patterns noticeable in back-  
248 scattered electron imaging, reflecting mild variations in  $\text{Mg}^{2+}/(\text{Fe}^{2+} + \text{Mg}^{2+})$  ratios (XMg)  
249 (**Supplementary Figure S1B**; see also **Figure S2**). The core of large white mica grains was  
250 targeted for dating, while the foliated matrix epidote was targeted for  $^{87}\text{Sr}/^{86}\text{Sr}$  determinations,  
251 since these are interpreted as part of an equilibrium assemblage.

## 252 **Metasomatic rinds, altered metagabbro and veins**

253 Samples SYGR37 and SYGR38 represent the matrix wrapping around metagabbro and  
254 blueschist blocks. These samples are coarse-grained, foliated schists composed mainly of  
255 glaucophane, epidote, phengite and chlorite. White mica from both metasomatic rinds are  
256 medium to coarse-grained and occur in sharp contact with glaucophane and epidote, displaying  
257 no significant chemical zoning patterns in major elements nor textural evidence of  
258 recrystallization (**Figures 2C and 2D**; see also **Figure S2**). Sharp contacts between white mica  
259 and epidote suggest textural equilibrium between them (**Supplementary Figure S1C**). Thus,  
260 we targeted these microdomains for white mica dating and  $^{87}\text{Sr}/^{86}\text{Sr}$  determinations.

261

262 Sample SYGR42 is an altered metagabbro composed of porphyroclasts of Na-Ca amphibole  
263 and omphacite after igneous clinopyroxene in a matrix of epidote, white mica and glaucophane  
264 (**Figure 2E**). Two generations of epidote, spatially associated with two distinct microdomains,  
265 are observed. The first epidote generation grew as fine-grained, now heavily smeared crystals  
266 occupying the interstitial matrix between porphyroclasts. This texture likely reflects epidote  
267 growth after igneous plagioclase and subsequent deformation. The second epidote generation  
268 grew in microdomains where a discontinuous foliation composed of tabular glaucophane and  
269 epidote in sharp contact with white mica, wrapped around porphyroclasts and the fine-grained  
270 epidote matrix. Within this second microdomain, white mica is medium- to coarse-grained and  
271 displays evidence of recrystallization and subgrains. For this reason, coarse-grained white mica  
272 crystals displaying no textural evidence for recrystallization, such as subgrains, kinks and  
273 undulose extinction, were carefully selected for dating, whereas euhedral and tabular epidote  
274 crystals in sharp contact with white mica crystals were targeted for  $^{87}\text{Sr}/^{86}\text{Sr}$  analysis.

275



276 Sample SYGR41 is a glaucophane + white mica dilational vein cross-cutting an omphacitite  
277 pod. These veins display up to centimeter-sized and randomly oriented laths of white mica  
278 (**Figure 2F**) displaying no evidence of deformation nor significant chemical zoning  
279 (**Supplementary Figure S1D**).

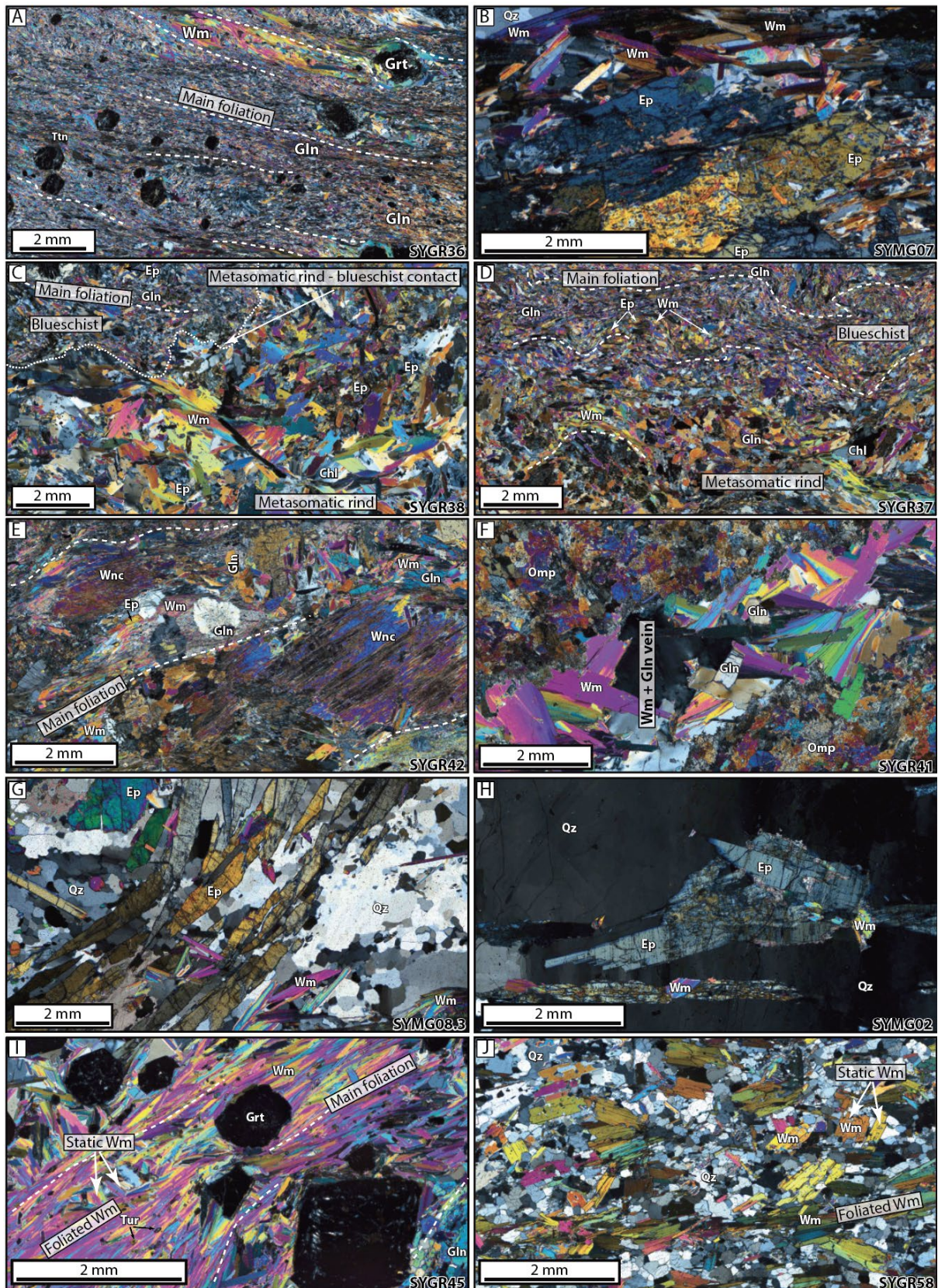
280  
281 Samples SYMG02 and SYMG08.3 are dilational veins crosscutting the foliated greenschist  
282 hosts. Elongated epidote crystals occur spatially associated with white mica in sharp contact  
283 suggesting contemporaneous precipitation from a fluid phase (**Figures 2G and 2H**). White  
284 mica occurs as euhedral, hundreds of  $\mu\text{m}$  long laths and correspond to strain free crystals with  
285 no to faint chemical zoning (**Supplementary Figures S1E and S1F**). Thus, the most coarse  
286 and pristine (e.g., unfractured) crystals were selected for white mica dating and epidote  
287  $^{87}\text{Sr}/^{86}\text{Sr}$  analyses.

## 288 **Metasedimentary rock and felsic pod**

289 Sample SYGR45 is a well foliated garnet, glaucophane, tourmaline, mica schist with minor  
290 epidote (**Figure 2I**). Texturally, the foliated white mica generation is apparently overgrown by  
291 a second, static generation characterized by laths oriented oblique to the main foliation (**Figure**  
292 **2E**). To avoid potentially retrograde rims, cores of large crystals defining the pervasive  
293 foliation and those of crystals oblique to it were targeted for dating. However, the resulting  
294 ages for these two white mica generations were indistinguishable within uncertainty, therefore  
295 the final age for this sample was calculated by clustering both datasets (see below).

296  
297 Sample SYGR58 is a felsic pod contained within the blueschist-facies meta-igneous breccia.  
298 They are composed mostly of quartz and phengite and subordinate epidote and garnet, the latter  
299 typically replaced by chlorite. A first white mica generation defines the foliation, whereas a  
300 second generation of laths are oriented oblique to it (**Figure 2J**). Although the two white mica  
301 generations were separately targeted for dating, the resulting ages overlap and were merged for  
302 the final sample age calculation (see below).

303  
304  
305  
306  
307  
308  
309  
310  
311



312  
 313  
 314  
 315  
 316  
 317  
 318

**Figure 2.** Photomicrographs (crossed polars) of the dated samples. *A.* General overview of the blueschist block sample SYGR36 emphasizing the distribution of white mica along the foliation and typically around garnets forming pressure shadows. *B.* General fabric of the greenschist sample SYMG07 displaying the association between foliated epidote and white mica. Due to the significant amount of inclusions within epidote, only the inclusion-free regions were targeted for laser ablation MC-ICP-MS analysis. *C.* Contact between altered blueschist and metasomatic rind in sample SYGR38; note the relatively curvy-sharp contact between these two

319 domains as well as the relatively larger abundance of coarse-grained white mica in the latter. D. Contact between  
320 altered blueschist and metasomatic rind in sample SYGR37. In this case, the contact is moderately- to highly-  
321 strained resulting in a more diffuse appearance. E. Metasomatized metagabbro sample SYGR42 displaying  
322 clinopyroxene pseudomorph porphyroclasts (now replaced by amphibole) in a foliated matrix composed of white  
323 mica, glaucophane and epidote. F. Dilational vein cross-cutting an omphacitite pod (sample SYGR41) with  
324 strain-free, millimeter-sized white mica crystals in association with glaucophane. G. Dilational white mica +  
325 epidote + quartz vein (sample SYMG08.3) with a texture characterized by epidote fibers and white mica laths. H.  
326 Dilational white mica + epidote + quartz vein (sample SYMG02) displaying coarse-grained epidote in sharp  
327 contact with finer-grained white mica. I. Metasedimentary rock sample SYGR45 highlighting white mica crystals  
328 oriented parallel and oblique (static) to the main foliation as well as developing pressure shadows around garnet.  
329 J. Felsic pod sample SYGR58 highlighting the distribution of white mica along the main foliation as well as some  
330 grains oriented oblique to it in a matrix of quartz.

## 331 **Methods**

### 332 **Laser ablation MC-ICP-MS**

333 In-situ Sr isotope analyses of epidote were undertaken in two separate sessions (March 2023  
334 and February 2024) using an ASI RESolution 193 nm excimer laser ablation system interfaced  
335 to a Nu Plasma II MC-ICP-MS at ETH Zürich following a similar approach from Fitzpayne et  
336 al. (2023) and Pimenta Silva et al. (2023). Analytical conditions included 80-100  $\mu\text{m}$  spot size,  
337 a repetition rate of 5 Hz (Mar-23) and 10 Hz (Feb-24), and laser fluence of  $\sim 4.0$  (Mar-23) and  
338  $2.5 \text{ J cm}^{-2}$  (Feb-24). Each analysis consisted of a sequence of 40 seconds of ablation and 15  
339 seconds of washout followed by 30 seconds of gas blank measurement. Total Sr signals varied  
340 widely from  $\sim 1$  to 15 V depending on the sample (**Supplementary Table S1**). Data reduction,  
341 including corrections for isobaric interferences (Kr, Ca dimers, Ca argides, Rb) and  
342 instrumental mass bias was performed using Iolite 4 (Paton et al., 2007, Paton et al., 2011).  
343 Instrumental drift was evaluated by repeated measurement of clinopyroxene BB-1 (Neumann  
344 et al., 2004; Fitzpayne et al., 2020), which was ablated every block of 15 unknowns including  
345 secondary clinopyroxene standards (JJG1414; YY09-04; YY09-47; YY12-01) from Zhao et  
346 al. (2020) (results included in **Supplementary Table S1**). All the data are reported relative to  
347 BB-1 of  $^{87}\text{Sr}/^{86}\text{Sr}$  of 0.704468 (Fitzpayne et al., 2020) via standard bracketing.  $^{84}\text{Sr}/^{86}\text{Sr}$  of  
348 clinopyroxene standards and epidote unknowns are generally within uncertainty of the natural  
349 ratio ( $\sim 0.0565$ ).  $^{87}\text{Rb}/^{86}\text{Sr}$  ratios are negligible (typically  $< 0.001$ ), which makes corrections for  
350  $^{87}\text{Sr}$  ingrowth insignificant. Therefore, the reported Sr isotope ratios are considered to be equal  
351 to the initial Sr isotope ratios at time of epidote crystallization.

### 352 **Laser ablation ICP-MS/MS**

353 In-situ Rb-Sr isotopic analyses of white mica in thin section were undertaken during two  
354 sessions (October 2022 and May 2023) using an ASI RESolution 193 nm excimer laser probe  
355 interfaced to an Agilent 8800 ICP-MS/MS at ETH Zürich following the procedure outlined in  
356 Giuliani et al. (2024) and Ceccato et al. (2024), which builds up on the pioneering work of  
357 Zack and Hogmalm (2016) and Hogmalm et al. (2017). The mass spectrometer was first tuned  
358 in single-quad mode (i.e. no gas in the collision cell) to optimize the Rb and Sr signals by  
359 ablating NIST612. Oxide production rate based on measurement of ThO/Th in NIST612 was

360  $\leq 0.2\%$ . After introducing ultrapure  $\text{N}_2\text{O}$  gas ( $>99.99\%$ ) in the reaction cell (flow rate of 0.23-  
361  $0.25\text{ mL min}^{-1}$ ), a second tuning step was undertaken by ablating NIST610 to maximize  
362 production of  $\text{SrO}^+$  ions while maintaining high sensitivity for  $\text{Rb}^+$  ions. Interaction of  $\text{Sr}^+$  ions  
363 with  $\text{N}_2\text{O}$  resulted in conversion of  $\sim 89\%$  of  $\text{Sr}^+$  ions to  $\text{SrO}^+$  based on monitoring of masses  
364 88 ( $\text{Sr}^+$ ), 104 ( $\text{SrO}^+$ ) and 105 ( $\text{SrOH}^+$ ). No  $\text{RbO}^+$  was detected. Analytical conditions for mica  
365 analyses included 80-100  $\mu\text{m}$  spot size, a pulse rate of 5 Hz, and laser fluence of  $\sim 3.5\text{-}4.0\text{ J cm}^{-2}$ .  
366 Each analysis consisted of a sequence of 40 seconds of ablation and 15 seconds of washout  
367 followed by 30 seconds of gas blank measurement. Dwell times were of 100 ms for  $^{85}\text{Rb}$ ,  
368  $^{86}\text{Sr}^{16}\text{O}$  and  $^{87}\text{Sr}^{16}\text{O}$ , 50 ms for  $^{86}\text{Sr}$  and  $^{87}(\text{Sr}+\text{Rb})$ , 20 ms for  $^{88}\text{Sr}$ ,  $^{88}\text{Sr}^{16}\text{O}$  and  $^{88}\text{Sr}^{16}\text{OH}$ , and  
369 10 ms for other elements (e.g., Ca, Ti, Ni, Ce, Yb, Th), which were monitored to assess  
370 potential contamination by extraneous material. Data reduction was performed using the “Rb-  
371 Sr isotopes” data reduction scheme in Iolite 4 (Paton et al., 2011). Instrumental drift and  
372 quantification of  $^{87}\text{Sr}/^{86}\text{Sr}$  and ‘uncorrected’  $^{87}\text{Rb}/^{86}\text{Sr}$  were undertaken by repeated ablation of  
373 NIST610, which was measured every block of 15 unknowns including in-house mica standards  
374 (see below). Natural glass standards BCR-2G and BHVO-2G were also analyzed as a quality  
375 measure of the Sr isotope analyses and returned values broadly consistent with accepted values  
376 (**Supplementary Table S2**). NIST610 is a synthetic glass with different ablation properties  
377 than mica and, therefore, this approach provides biased (i.e. ‘uncorrected’)  $^{87}\text{Rb}/^{86}\text{Sr}$  ratios in  
378 mica analyses (e.g., Redaa et al., 2021). Correction of NIST610-based ‘uncorrected’  $^{87}\text{Rb}/^{86}\text{Sr}$   
379 in the mica unknowns was performed following the method outlined by Giuliani et al. (2024).  
380 The calculated age of an in-house mica standard from the Wimbledon kimberlite (South  
381 Africa), which has a robustly constrained Rb-Sr age of  $114.5 \pm 0.8\text{ Ma}$  ( $2\sigma$ ) based on isotope  
382 dilution analyses (Sarkar et al., 2023) and exhibits large variation in Rb/Sr (almost 3 orders of  
383 magnitude), was employed to calculate a correction factor that is then employed to obtain the  
384 final  $^{87}\text{Rb}/^{86}\text{Sr}$  in the mica unknowns. The validity of this approach was confirmed by analyses  
385 of micas from the Bultfontein kimberlite (South Africa) and Mount Dromedary monzonite  
386 (MD-2; Australia) which returned Rb-Sr ages that are indistinguishable from solution-mode  
387 Rb-Sr and Ar-Ar analyses of mica on the same sample:  $88.3 \pm 0.2\text{ Ma}$  (Fitzpayne et al., 2020),  
388 and  $99.20 \pm 0.08\text{ Ma}$  (Phillips et al., 2017), respectively (**Supplementary Table S2**). Time-  
389 resolved spectra of mica unknowns and reference materials were screened to remove  
390 anomalous regions based on e.g., low concentrations of Rb and high concentrations of Sr, Ca,  
391 Ce and/or other incompatible trace elements. Analyses with total signals of less than 10 seconds  
392 (after screening) and with anomalously low contents of Rb or high contents of Sr (and Ca),  
393 often resulting in  $^{87}\text{Rb}/^{86}\text{Sr} < 2.5$ , as well as analyses with large  $^{87}\text{Sr}/^{86}\text{Sr}$  uncertainties and data  
394 points that plotted distinctly off the isochron were not included in the Nicolaysen diagrams  
395 (**Supplementary Table S3**). All the isochron ages were calculated using IsoplotR (Vermeesch,  
396 2018) and the  $^{87}\text{Rb}$  decay constant of  $1.3972 \times 10^{-11}\text{ a}^{-1}$  (Villa et al., 2015). Trace element  
397 concentrations were not quantified.  
398

# Results

## 400 Epidote Sr isotopes

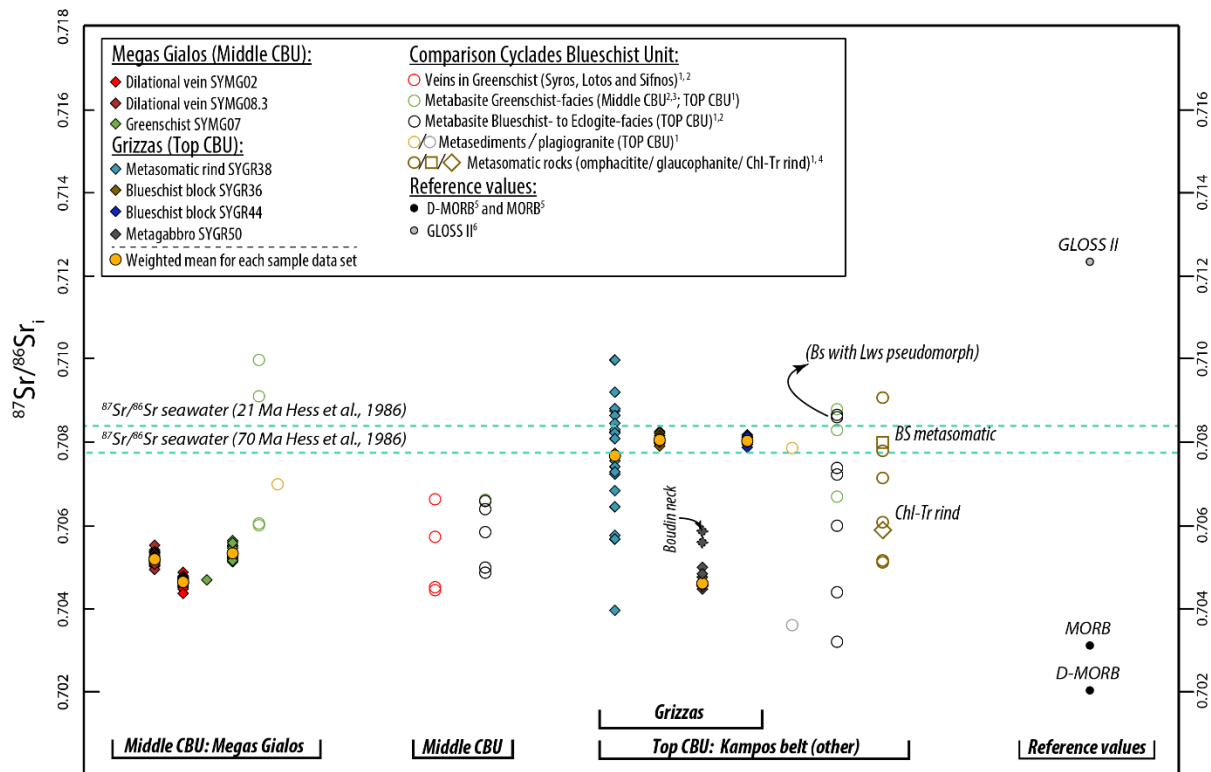
401 The  $^{87}\text{Sr}/^{86}\text{Sr}$  ratios were measured by laser ablation MC-ICP-MS in 5 of the 10 samples  
402 employed for mica Rb-Sr geochronology. Two additional samples (SYGR44; SYGR50) were  
403 also included to corroborate the signature of the blueschist and metagabbro rocks. For  
404 comparison, we also present isotope-dilution Sr isotope data in samples from the Megas Gialos  
405 locality, including the 3 samples analyzed for epidote and mica Rb-Sr isotopes. A summary of  
406 the new and available Sr isotope data for epidote is reported in **Figure 3** and the full datasets,  
407 including bulk rock Sr and Nd isotopic compositions, are included in **Supplementary Tables**  
408 **S1 and S4**.

409

410 At Grizzas (Kampos belt), the two blueschist samples (SYGR36 and 44) show very small  
411 ranges in epidote  $^{87}\text{Sr}/^{86}\text{Sr}$  compositions (see **Supplementary Figure S3**) with  
412 indistinguishable weighted means of  $0.70805 \pm 0.00006$  (2SE;  $n = 12$ ) and  $0.70802 \pm 0.00005$   
413 (2SE;  $n = 18$ ; **Table 2 and Supplementary Figure S3**). The other two Grizzas samples (the  
414 metasomatic rind SYGR38 and the metagabbro SYGR50) exhibit larger isotopic variability.  
415 The  $^{87}\text{Sr}/^{86}\text{Sr}$  in sample SYGR38 vary widely between  $0.70426 \pm 0.00008$  and  $0.710002 \pm$   
416  $0.00008$  ( $n = 22$ ) with no statistically distinct populations (**Figure 3**). The weighted mean  
417 (although statistically meaningless) is similar to those of SYGR36 and SYGR44:  $0.70767 \pm$   
418  $0.00058$ . In sample SYGR50, 16 epidote grains parallel to the foliation yield a restricted range  
419 in Sr isotope values corresponding to a weighted mean of  $0.70460 \pm 0.00004$ , which is  
420 substantially less radiogenic than the blueschist samples from Grizzas, although similar to the  
421 lowest  $^{87}\text{Sr}/^{86}\text{Sr}$  of sample SYGR38. Four epidote grains within boudin necks of sample  
422 SYGR50 show more radiogenic values of up to  $0.70585 \pm 0.00020$ .

423

424 Epidote in the three samples from Megas Gialos show very limited within-sample  $^{87}\text{Sr}/^{86}\text{Sr}$   
425 variability with weighted means of  $0.70466 \pm 0.00004$  ( $n = 24$ ) for SYMG02;  $0.70534 \pm$   
426  $0.00005$  ( $n = 25$ ) for SYMG07 and  $0.70520 \pm 0.00005$  ( $n = 31$ ) for SYMG08.03 The epidote  
427 Sr isotope compositions are not correlated with the lithology as the greenschist sample  
428 SYMG07 has the same  $^{87}\text{Sr}/^{86}\text{Sr}$  as one of the two dilational veins (SYMG02 and 08.03).  
429 Measured (i.e. present-day)  $^{87}\text{Sr}/^{86}\text{Sr}$  of bulk rock SYMG07 is  $0.705414 \pm 0.000008$  ( $2\sigma$  s.d. of  
430 NBS987 standards measured in the same session), marginally more radiogenic than the  
431 SYMG07 epidote, and minimally affected by radiogenic ingrowth (e.g.,  $\sim 0.0002$  in 50 Myr)  
432 due to low bulk-rock  $^{87}\text{Rb}/^{86}\text{Sr}$  of 0.290 (**Supplementary Table S1**). The bulk-rock  $^{87}\text{Sr}/^{86}\text{Sr}$   
433 of SYMG08.03 ( $0.705281 \pm 0.000006$ ) is almost indistinguishable from the epidote value  
434 reported above. The very low  $^{87}\text{Rb}/^{86}\text{Sr}$  (0.073) suggests minimal radiogenic Sr ingrowth in  
435 this bulk sample.



436  
 437 **Figure 3.** Overview of  $^{87}\text{Sr}/^{86}\text{Sr}$  in-situ laser ablation MC-ICP-MS epidote data points and comparison to ID-  
 438 TIMS (whole rock and multi-mineral) analyses from different localities in Syros. The resulting  $^{87}\text{Sr}/^{86}\text{Sr}$  values  
 439 are assumed to represent initial ratios due to the lack of Rb in epidote. For comparison, pristine MORB and D-  
 440 MORB, as well as compiled trench filling sediments (GLOSS II) along with Cretaceous to Miocene  $^{87}\text{Sr}/^{86}\text{Sr}$   
 441 seawater values are shown. Uncertainties are smaller than the symbol size. 1 – Glodny and Ring (2022); 2 –  
 442 Kotowski et al. (2022); 3 – Bröcker et al. (2013); 4 – Bröcker and Enders (2001); 5 – Salters and Stracke (2004);  
 443 6 – Plank (2014).

## 444 Mica Rb-Sr dating

445 In this section we report the mica Rb-Sr isotope data and describe the related isochronous array  
 446 for each sample, complemented in 5 cases by epidote Sr isotope results. The complete white  
 447 mica dataset, including Rb and Sr isotope ratios, is provided in **Supplementary Table S3** (see  
 448 **Table 2** for a summary of the age data). For each sample we also provide a model age where  
 449 the mica Rb-Sr isochron is anchored to an assumed  $^{87}\text{Sr}/^{86}\text{Sr}$  value, that is  $0.7080 \pm 0.0005$  for  
 450 all the samples from Grizzas, and  $0.7050 \pm 0.0005$  for those from Megas Gialos. For Grizzas,  
 451 employing this value is justified by the fact that the weighted mean of epidote Sr isotopes are  
 452  $\sim 0.708$  for three of the four analyzed samples (**Figure 3**; see also the compiled data in **Figure**  
 453 **3** for metabasites from the Top CBU), and “unanchored” mica Rb-Sr isochrons are generally  
 454 within uncertainty of this value (see below). The epidote and bulk-rock compositions at Megas  
 455 Gialos cluster at  $^{87}\text{Sr}/^{86}\text{Sr}$  of  $\sim 0.705$  (**Figure 3**) hence providing a robustly constrained initial  
 456 Sr composition for anchoring the mica-based Nicolaysen arrays. In the discussion section, we  
 457 will address the impact of changing initial (or “common”)  $^{87}\text{Sr}/^{86}\text{Sr}$  composition in the  
 458 calculated Rb-Sr isochron.

459 **SYGR36**

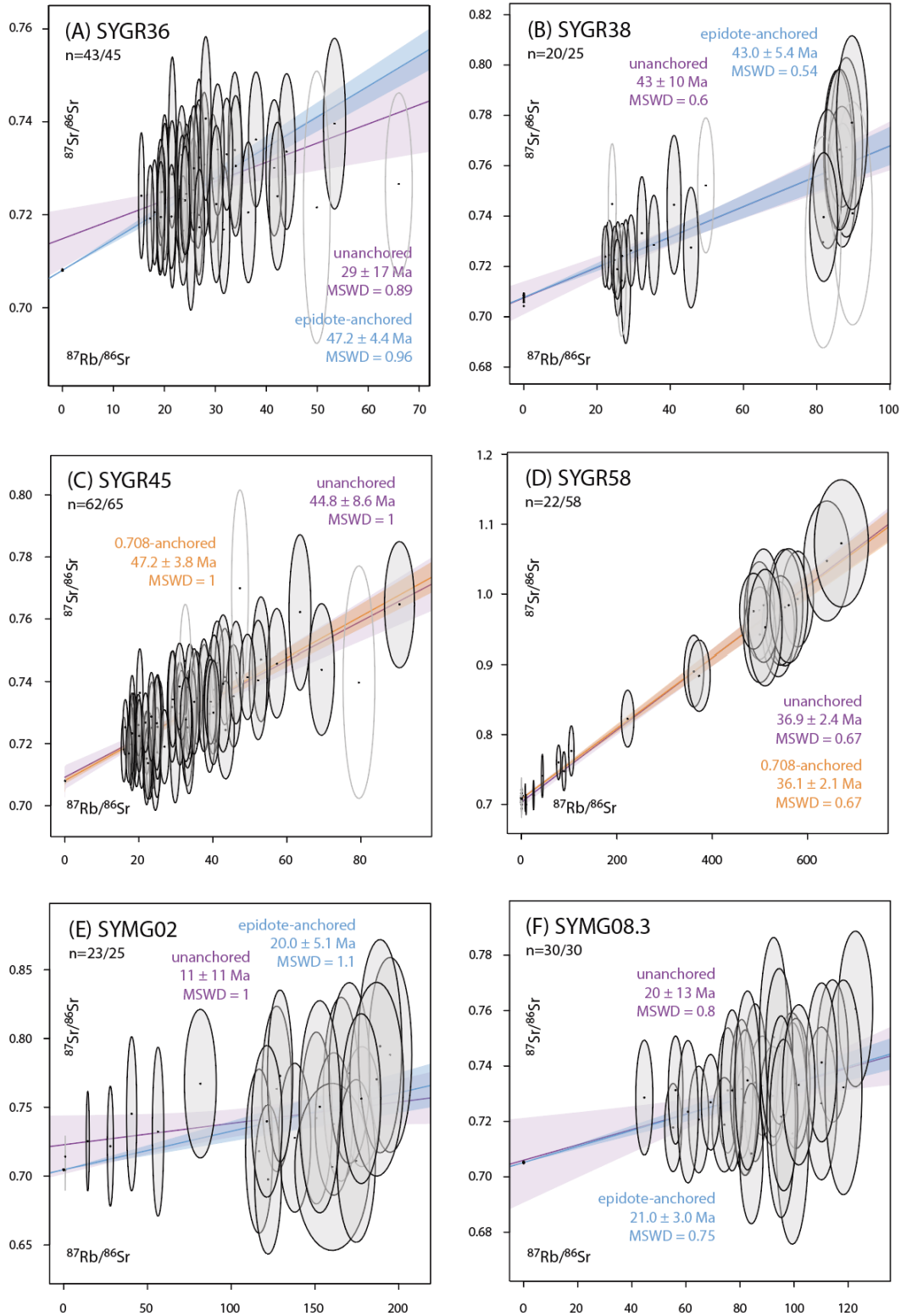
460 White mica in the blueschist block sample SYGR36 show a spread in  $^{87}\text{Rb}/^{86}\text{Sr}$  between 15  
461 and 53 ( $n = 43/45$ ) associated with variations in  $^{87}\text{Sr}/^{86}\text{Sr}$  between 0.7166 and 0.7407 (**Figure**  
462 **4A**). The limited Rb/Sr spread results in a poorly defined “unanchored” isochron age of  $29 \pm$   
463  $17$  Ma (2SE, MSWD = 0.89, initial  $^{87}\text{Sr}/^{86}\text{Sr} = 0.7149 \pm 0.0062$ ). Anchoring the phengite Rb-  
464 Sr data to epidote from the same sample (weighted mean  $^{87}\text{Sr}/^{86}\text{Sr} = 0.70805 \pm 0.00006$ )  
465 provides a rather different (although within uncertainty) and considerably more precise age of  
466  $47.2 \pm 4.4$  Ma (2SE, MSWD = 0.96). Assuming a modeled initial  $^{87}\text{Sr}/^{86}\text{Sr}$  of  $0.7080 \pm 0.0005$   
467 (1s) provides an age of  $46.9 \pm 5.1$  Ma (2s, MSWD = 0.96), overlapping closely with the epidote-  
468 anchored isochron age.

469 **SYGR37**

470 White mica grains in the metasomatic rind sample SYGR37 show a slightly larger spread in  
471  $^{87}\text{Rb}/^{86}\text{Sr}$  (22-112,  $n = 36/38$ ) and  $^{87}\text{Sr}/^{86}\text{Sr}$  (0.7211-0.7676) compared to SYGR36, resulting  
472 in a more precise unanchored isochron age of  $32.3 \pm 7.5$  Ma (MSWD = 0.51, initial  $^{87}\text{Sr}/^{86}\text{Sr} =$   
473  $0.7158 \pm 0.0059$ ; **Supplementary Figure S4**). Anchoring these mica Rb-Sr to modeled initial  
474  $^{87}\text{Sr}/^{86}\text{Sr}$  of  $0.7080 \pm 0.0005$  (2SE) yields an older age of  $41.1 \pm 3.1$  Ma (MSWD = 0.66).

475 **SYGR38**

476 White mica in the metasomatic rind SYGR38 shows spreads between 22-90 and 0.7140-0.7771  
477 for  $^{87}\text{Rb}/^{86}\text{Sr}$  and  $^{87}\text{Sr}/^{86}\text{Sr}$ , respectively ( $n = 20/25$ , with 5 analyses excluded based on short  
478 signals of less than 10 seconds). The corresponding unanchored isochron age is  $43 \pm 10$  Ma  
479 (MSWD = 0.6, initial  $^{87}\text{Sr}/^{86}\text{Sr} = 0.7075 \pm 0.0064$ ; **Figure 4B**). Adding epidote Sr isotopes  
480 (weighted mean  $^{87}\text{Sr}/^{86}\text{Sr} = 0.70767 \pm 0.00058$  (2SE)) to the mica Rb-Sr isochron yields the  
481 same, yet more precise age of  $43.0 \pm 5.4$  Ma (MSWD = 0.54). Using a modeled initial  $^{87}\text{Sr}/^{86}\text{Sr}$   
482 of  $0.7080 \pm 0.0005$  (2SE) results in a similar age of  $42.5 \pm 5.5$  Ma (MSWD = 0.54). Considering  
483 the large spread in epidote  $^{87}\text{Sr}/^{86}\text{Sr}$  values ( $\sim 0.7043$  to  $\sim 0.7100$ ), we have also calculated  
484 model ages using initial  $^{87}\text{Sr}/^{86}\text{Sr}$  of 0.7050 and 0.7100 and these are within uncertainty of each  
485 other:  $46.5 \pm 5.6$  Ma (MSWD = 0.57) and  $39.8 \pm 5.5$  Ma (MSWD = 0.57), respectively  
486 (**Supplementary Figure S5**).



487  
 488 **Figure 4.** Representative laser-ablation ICP-MS/MS Rb-Sr isochrons of white micas from Grizzas (North East  
 489 Syros Island, SYGR, A-D) and Megas Gialos (South Syros Island, SYMG, E-F). The size of the ellipses represents  
 490 internal 2 SE (standard error), where data points that were excluded from the regression are displayed as empty  
 491 ellipses. Isochronous regressions are plotted together with their 95% confidence level envelopes in different  
 492 colours based on the employed anchoring technique: purple for mica-only unanchored regressions; blue for  
 493 regressions anchored to epidote; orange for regressions anchored to a modelled initial  $^{87}\text{Sr}/^{86}\text{Sr}$  of  $0.7080 \pm$   
 494  $0.0005$ . The number below the sample labels indicates the number of mica analyses. All plots were generated  
 495 using IsoplotR (Vermeesch, 2018).  
 496



497 **SYGR41**

498 White mica from the dilational vein SYGR41 show a limited spread in  $^{87}\text{Rb}/^{86}\text{Sr}$  between 14-  
499 63 ( $n = 36/36$ ) associated with variations in  $^{87}\text{Sr}/^{86}\text{Sr}$  between 0.7116 and 0.7498. An  
500 unanchored isochron through these data yields an age of  $45 \pm 11$  Ma (MSWD = 0.78, initial  
501  $^{87}\text{Sr}/^{86}\text{Sr} = 0.7076 \pm 0.0049$ ). Anchoring these mica Rb-Sr data to a modeled initial  $^{87}\text{Sr}/^{86}\text{Sr}$  of  
502  $0.7080 \pm 0.0005$  (1s) yields the same, yet more precise age of  $44.7 \pm 4.5$  Ma (2s, MSWD =  
503 0.74).  
504

505 **SYGR42**

506  $^{87}\text{Rb}/^{86}\text{Sr}$  and  $^{87}\text{Sr}/^{86}\text{Sr}$  ratios in phengites from the metasomatized metagabbro sample  
507 SYGR42 range from 27 to 185 and 0.7155 to 0.8162, respectively ( $n = 30/30$ ), and the  
508 corresponding unanchored isochrons provides an age of  $46 \pm 9$  Ma (MSWD = 1.3, initial  
509  $^{87}\text{Sr}/^{86}\text{Sr} = 0.7090 \pm 0.0079$ ). Anchoring these mica Rb-Sr data to  $^{87}\text{Sr}/^{86}\text{Sr} = 0.7080 \pm 0.0005$   
510 (1s) results in an overlapping, although more precise age of  $46.6 \pm 4.6$  Ma (MSWD = 1.2).  
511

512 **SYGR45**

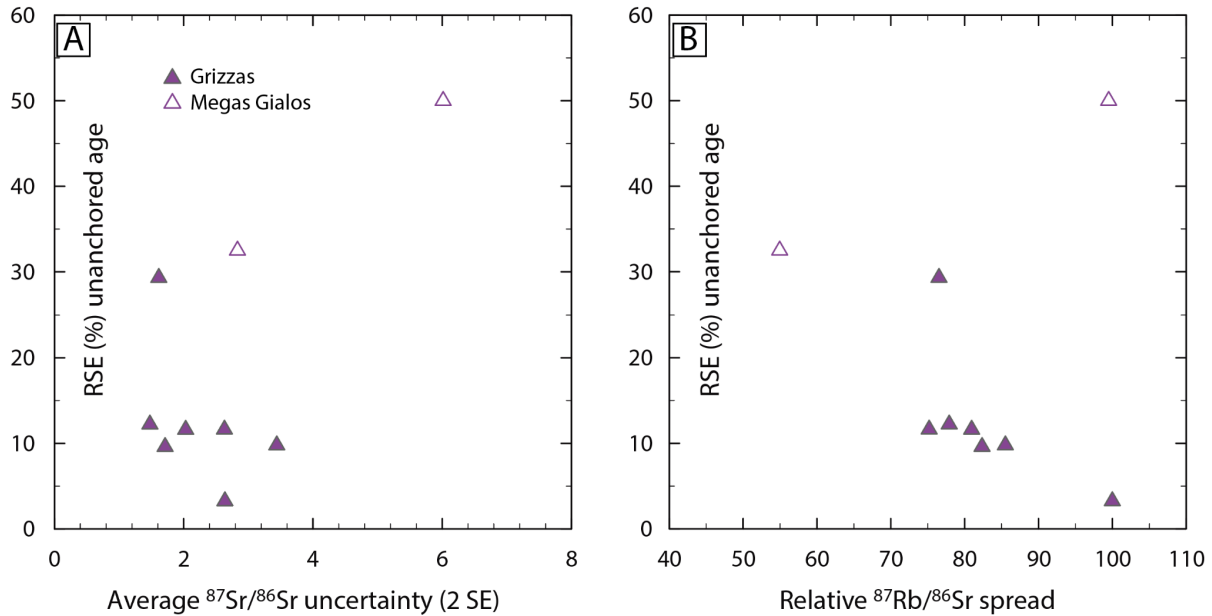
513 Two generations of phengite laths, parallel and oblique to the main foliation, from the  
514 metasedimentary rock sample SYGR45 display  $^{87}\text{Rb}/^{86}\text{Sr}$  values between 16 and 90 ( $n = 62/65$ )  
515 and a corresponding variation in  $^{87}\text{Sr}/^{86}\text{Sr}$  between 0.7134 and 0.7647, with no systematic  
516 difference between the two textural types of mica (**Figure 4C**; **Supplementary Table S3**). The  
517 resulting unanchored isochron has a slope equivalent to an age of  $44.8 \pm 8.6$  Ma (MSWD = 1,  
518 initial  $^{87}\text{Sr}/^{86}\text{Sr} = 0.7092 \pm 0.0038$ ). Anchoring these mica Rb/Sr data to a modeled initial  
519  $^{87}\text{Sr}/^{86}\text{Sr}$  of  $0.7080 \pm 0.0005$  (1s) yields a slightly older and more precise age of  $47.2 \pm 3.8$  Ma  
520 (MSWD = 1), overlapping with the unanchored age within uncertainty. Using a more  
521 radiogenic initial  $^{87}\text{Sr}/^{86}\text{Sr}$  of 0.7100 has a small effect on the calculated age ( $43.2 \pm 3.8$ ;  
522 MSWD = 1).  
523

524 **SYGR58**

525 The two textural types of white mica identified in the felsic pod sample SYGR58, parallel and  
526 oblique to the main foliation, exhibit indistinguishable Rb-Sr isotope systematics  
527 (**Supplementary Table S3**) and are, hence, described together. These white micas show the  
528 largest Rb/Sr spread observed in the sample set of between 8 and 671 ( $n = 22/58$ , where only  
529 analyzes with  $^{87}\text{Rb}/^{86}\text{Sr} > 2.5$  were considered for the isochron), which is consistent with the  
530 felsic nature of this sample. The spread in  $^{87}\text{Sr}/^{86}\text{Sr}$  is between 0.670 and 1.073, resulting in  
531 precise, although unanchored Rb-Sr age of  $36.9 \pm 2.4$  Ma (MSWD = 0.67, initial  $^{87}\text{Sr}/^{86}\text{Sr} =$   
532  $0.7038 \pm 0.0072$ ; **Figure 4D**). Anchoring these mica Rb/Sr data to a modeled initial  $^{87}\text{Sr}/^{86}\text{Sr}$   
533 of  $0.7080 \pm 0.0005$  (2SE) yields a similar age of  $36.1 \pm 2.1$  Ma (2s, MSWD = 0.67).  
534

## 535 SYMG02

536 Phengites from the dilational vein sample SYMG02 show a relatively large  $^{87}\text{Rb}/^{86}\text{Sr}$  spread  
537 between 14 and 195 ( $n = 23/25$ ) associated with a restricted  $^{87}\text{Sr}/^{86}\text{Sr}$  spread between 0.6976  
538 and 0.7944. These data define a meaningless unanchored isochron (age =  $11 \pm 11$  Ma, MSWD  
539 = 1, initial  $^{87}\text{Sr}/^{86}\text{Sr} = 0.723 \pm 0.021$ ; **Figure 4E**). Adding epidote Sr data from the same sample  
540 (weighted mean  $^{87}\text{Sr}/^{86}\text{Sr} = 0.70466 \pm 0.00004$ ) to the mica Rb-Sr isotopes results in a more  
541 meaningful age of  $20.0 \pm 5.1$  Ma (MSWD = 1.1). Using a modeled initial  $^{87}\text{Sr}/^{86}\text{Sr}$  anchor of  
542  $0.7050 \pm 0.0005$  (1s) yields a similar age of  $19.8 \pm 5.2$  Ma (2s, MSWD = 1).



543

544 **Figure 5.** Comparison of relative standard error (RSE) of unanchored mica Rb-Sr ages and (A) average  $^{87}\text{Sr}/^{86}\text{Sr}$   
545 uncertainties and (B) relative (%)  $^{87}\text{Rb}/^{86}\text{Sr}$  spread. The latter was defined as the ratio between the absolute  
546  $^{87}\text{Rb}/^{86}\text{Sr}$  spread and the highest  $^{87}\text{Rb}/^{86}\text{Sr}$  value observed for any given sample, resulting in a number between 0  
547 and 100%.

## 548 SYMG07

549  $^{87}\text{Rb}/^{86}\text{Sr}$  and  $^{87}\text{Sr}/^{86}\text{Sr}$  values in white mica from the greenschist sample SYMG07 vary  
550 between 75-231 and 0.7199-0.8121, respectively ( $n = 12/13$ ), yielding a meaningless isochron  
551 age of  $6.1 \pm 31.2$  Ma (MSWD = 1.2, initial  $^{87}\text{Sr}/^{86}\text{Sr} = 0.749 \pm 0.063$ ; **Supplementary Figure**  
552 **S4**). Coupling white mica with the SYMG07 epidote data (weighted mean  $^{87}\text{Sr}/^{86}\text{Sr} = 0.70534$   
553  $\pm 0.00005$ ) results in an age of  $27.2 \pm 8.4$  Ma (MSWD = 1.1). An identical age is obtained  
554 using a model initial  $^{87}\text{Sr}/^{86}\text{Sr}$  of  $0.7050 \pm 0.0005$  (1s):  $27.4 \pm 8.4$  Ma (2s, MSWD = 1.2).  
555

## 556 SYMG08

557 Phengites from dilational vein SYMG08.3 show a spread in  $^{87}\text{Rb}/^{86}\text{Sr}$  between 45 and 123 ( $n = 30/30$ )  
558 associated with variations in  $^{87}\text{Sr}/^{86}\text{Sr}$  between 0.7084 and 0.7606 (**Figure 4F**). These  
559 data define an unanchored isochron age of  $20 \pm 13$  Ma (MSWD = 0.8, initial  $^{87}\text{Sr}/^{86}\text{Sr} = 0.706$   
560  $\pm 0.015$ ). Adding Sr epidote data (weighted mean  $^{87}\text{Sr}/^{86}\text{Sr} = 0.70520 \pm 0.00005$ ) to the  
561 phengite Rb/Sr data results in the same, yet more precise age of  $21.0 \pm 3.0$  Ma (MSWD = 0.75).

562 The results hardly change by anchoring the mica Rb/Sr data to a modeled initial  $^{87}\text{Sr}/^{86}\text{Sr}$  of  
 563  $0.7050 \pm 0.0005$  (2SE):  $20.8 \pm 3.1$  Ma (MSWD = 0.75) (**Supplementary Figure S5**).  
 564

Sample ID	Epidote $^{87}\text{Sr}/^{86}\text{Sr}$ *			Mica analyses		Mica age, unanchored **				Mica + epidote age (Ma)			Mica age (Ma), anchored ***		
	n	mean	2 SE	n	age (Ma)	2 SE	MSWD	isochron $\gamma$	intercept	age (Ma)	2 SE	MSWD	age (Ma)	2 SE	MSWD
<i>Grizzas (NE Syros)</i>															
SYGR36	12	0.70805	0.00006	43/45	<b>29</b>	17	0.89		$0.7149 \pm 0.0062$	<b>47.2</b>	4.4	0.96	<b>46.9</b>	5.1	0.96
SYGR37	–	–	–	36/38	<b>32.3</b>	7.5	0.51		$0.7158 \pm 0.0059$	–	–	–	<b>41.1</b>	3.1	0.66
SYGR38	21	0.70767	0.00058	20/25	<b>43</b>	10	0.60		$0.7075 \pm 0.0064$	<b>43.0</b>	5.4	0.54	<b>42.5</b>	5.5	0.54
SYGR41	–	–	–	36/36	<b>45</b>	11	0.78		$0.7076 \pm 0.0049$	–	–	–	<b>44.7</b>	4.5	0.74
SYGR42	–	–	–	30/30	<b>46</b>	9	1.30		$0.7090 \pm 0.0079$	–	–	–	<b>46.6</b>	4.6	1.2
SYGR44	18	0.70802	0.00005	–	–	–	–		–	–	–	–	–	–	–
SYGR45	–	–	–	62/65	<b>44.8</b>	8.6	1.00		$0.7092 \pm 0.0038$	–	–	–	<b>47.2</b>	3.8	1
SYGR50	16	0.70460	0.00004	–	–	–	–		–	–	–	–	–	–	–
SYGR58	–	–	–	22/58	<b>36.9</b>	2.4	0.67		$0.7038 \pm 0.0072$	–	–	–	<b>36.1</b>	2.1	0.67
<i>Megas Gialos (SE Syros)</i>															
SYMG02	24	0.70466	0.00004	23/25	<b>11</b>	11	1.00		$0.723 \pm 0.021$	<b>20.0</b>	5.1	1.1	<b>19.8</b>	5.2	1
SYMG07	25	0.70534	0.00005	12/13	<b>6.4</b>	31.2	1.20		$0.749 \pm 0.063$	<b>27.2</b>	8.4	1.1	<b>27.4</b>	8.4	1.2
SYMG08.3	31	0.70520	0.00005	30/30	<b>20</b>	13	0.80		$0.706 \pm 0.015$	<b>21.0</b>	3.0	0.75	<b>20.8</b>	3.1	0.75

\* laser ablation, multi-collector ICP-MS; complete dataset in Supplementary Table S1  
 \*\* laser ablation, ICP-MS/MS; complete dataset in Supplementary Table S3  
 \*\*\* anchoring values:  $0.7080 \pm 0.0005$  for SYGR samples;  $0.7050 \pm 0.0005$  for SYMG samples

565  
 566

## 567 Discussion

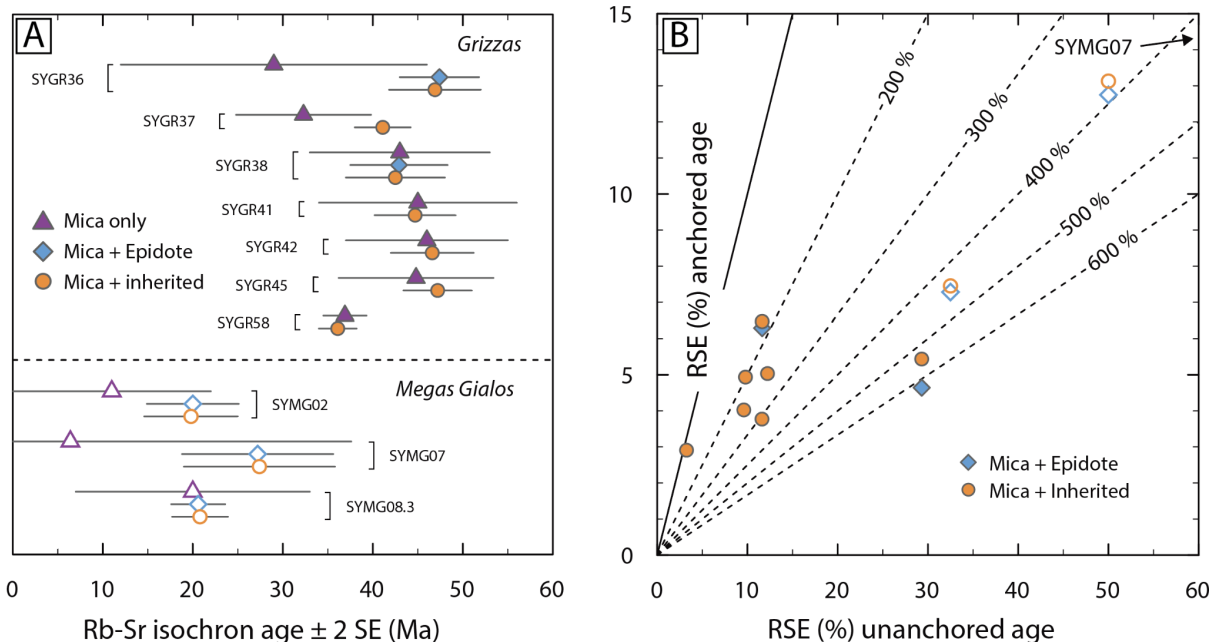
### 568 Optimal strategies to obtain robust Rb-Sr ages of white 569 mica in young metamorphic rocks by LA-ICP-MS/MS

570 White mica in all the investigated samples, and regardless of their bulk-rock chemistry (i.e.  
 571 mafic and metasomatic), exhibit limited spread in Rb/Sr compared to previous studies (e.g.,  
 572 Kirkland et al., 2023, Glodny and Ring 2022). Except for the relatively large spread observed  
 573 in the felsic sample SYGR58 ( $^{87}\text{Rb}/^{86}\text{Sr} = 8$  to  $671$ ), the Rb/Sr range of all the other samples  
 574 never exceeds one order of magnitude and in some cases less (e.g.,  $^{87}\text{Rb}/^{86}\text{Sr} = 15$ - $53$  in  
 575 blueschist SYGR36) compared to, for example, the two to three orders of magnitude in  
 576 phlogopite from lamproites and kimberlites (Giuliani et al., 2024), or biotite in some  
 577 metamorphosed granites (Ceccato et al., 2024). In addition, the combination of relatively low  
 578 Rb contents (not quantified but inferred from low Rb/Sr ratios) and geologically young  
 579 (Cenozoic) age of the Syros micas did not allow the ingrowth of substantial radiogenic  $^{87}\text{Sr}$  as  
 580 shown by the low measured  $^{87}\text{Sr}/^{86}\text{Sr}$  (generally  $<0.8$ ; **Supplementary Table S3**). Low  $^{87}\text{Sr}$   
 581 contents are associated with large uncertainties for  $^{87}\text{Sr}/^{86}\text{Sr}$ , which systematically exceed 1%  
 582 (2SE) for individual measurements (**Supplementary Table S3**). The compounded effects of  
 583 low absolute  $^{87}\text{Rb}/^{86}\text{Sr}$  values (generally  $<200$  and, for some samples,  $<100$ ), limited spread in  
 584 Rb/Sr and poor precision in the quantification of  $^{87}\text{Sr}/^{86}\text{Sr}$  result in large uncertainties  
 585 associated with the slopes of unanchored mica Rb-Sr isochrons (**Figure 5A and 5B**). These  
 586 uncertainties translate to a poor precision for the related ages with 10-29 %RSE (relative  
 587 standard error) in the SYGR samples (except for the felsic sample SYGR58, with an RSE of  
 588 3%, i.e.  $36.9 \pm 2.4$  Ma, 2SE), and even larger for the younger SYMG samples (**Figure 6A**).  
 589 The inverse correlation between relative  $^{87}\text{Rb}/^{86}\text{Sr}$  spread and age uncertainty of unanchored  
 590 isochrons in **Figure 5B** exemplifies the impact of Rb/Sr variations on isochron precision. In at

591 least three cases (SYGR36, SYMG02 and SYMG07) these unanchored mica-only isochronous  
 592 arrays are not just imprecise, but also rather inaccurate as shown by the substantially older ages  
 593 of the mica + epidote isochron for SYGR36 ( $29 \pm 17$  Ma vs  $47.2 \pm 4.4$  Ma for SYGR36) or  
 594 simply geologically meaningless ( $11 \pm 11$  Ma and  $6.4 \pm 31$  Ma for SYMG02 and SYMG07,  
 595 respectively; **Table 2**).

596

597 To overcome the limitations in mica Rb-Sr geochronology by LA-ICP-MS/MS due to low  
 598 Rb/Sr and/or young ages, the two viable solutions explored here include anchoring the  
 599 isochronous arrays to either the Sr isotope composition of a low Rb/Sr phase in textural  
 600 equilibrium with mica, such as epidote, or an assumed  $^{87}\text{Sr}/^{86}\text{Sr}$  value. The latter approach  
 601 effectively provides a “model age” and, while previously explored by Rösler and Zack (2021),  
 602 it is rigorously evaluated herein by a systematic comparison with initial Sr isotope constraints  
 603 from epidote and bulk rocks. Anchoring mica isochrons to a low Rb/Sr phase has been rarely  
 604 applied in mica Rb-Sr geochronology by LA-ICP-MS/MS (Ribeiro et al., 2022; Barnes et al.,  
 605 2024; Giuliani et al., 2024), while being widely employed for conventional Rb-Sr dating by  
 606 isotope dilution (e.g., Maas, 2003; Glodny et al., 2008; Hyppolito et al., 2016; Angiboust et al.,  
 607 2018; Dalton et al., 2020). Comparisons of unanchored mica Rb-Sr ages with those anchored  
 608 using mean  $^{87}\text{Sr}/^{86}\text{Sr}$  of epidote analyses show an improvement in precision of up to 6 times  
 609 (**Figure 6B**) – as well as better accuracy in some cases as shown above for SYGR36. Clearly,  
 610 in young HP metamafic rocks such as those from Syros, this approach is recommended to  
 611 obtain robust age constraints even when the limited spread in mica Rb/Sr prevents generation  
 612 of meaningful isochronous arrays (i.e. SYMG02 and 07).



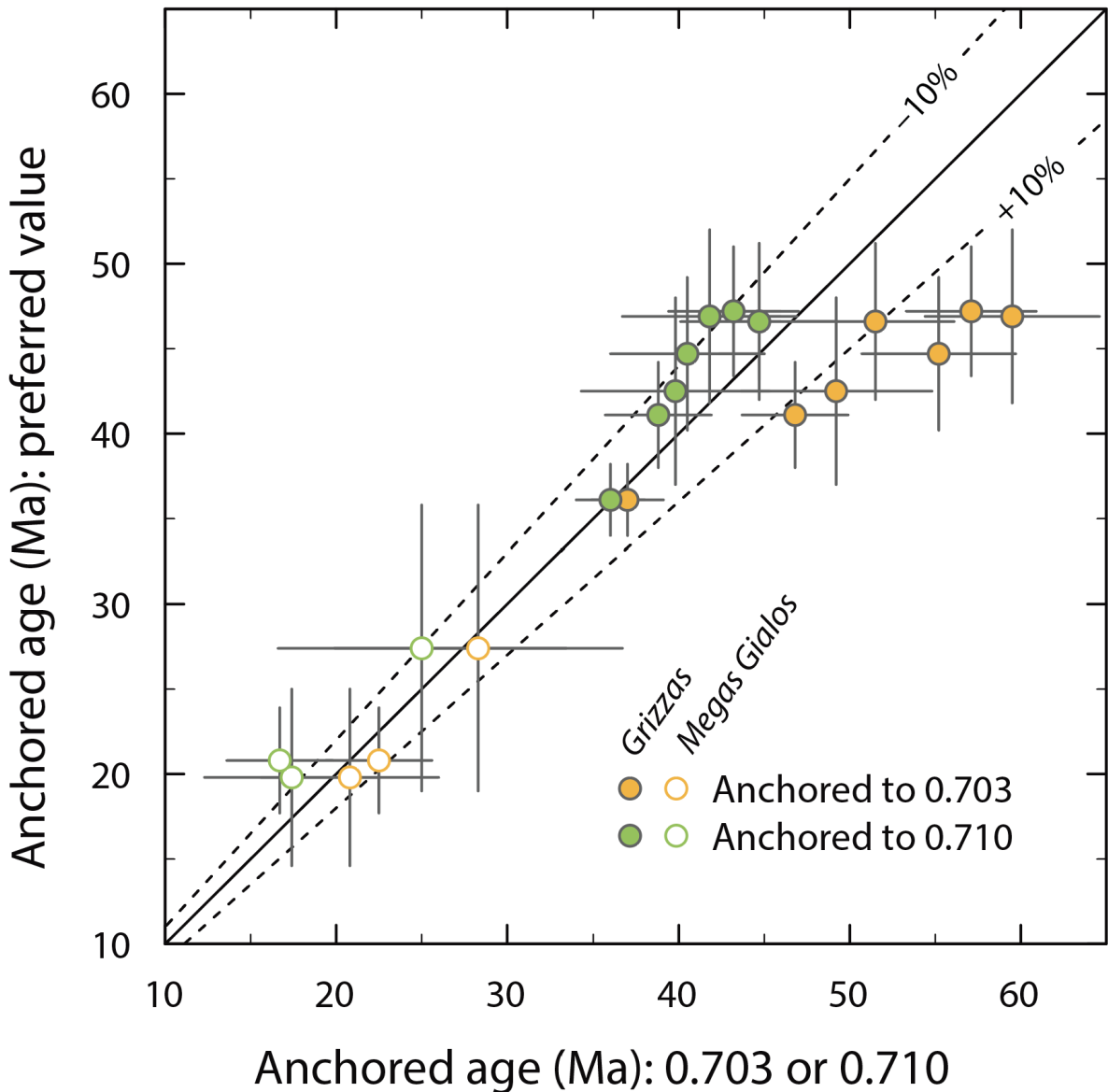
613

614 **Figure 6.** (A) Overview of mica Rb-Sr ages using mica datapoints only (unanchored isochrons, purple), anchoring  
 615 to epidote (blue) and anchoring to an assumed initial  $^{87}\text{Sr}/^{86}\text{Sr}$  composition (orange). Initial  $^{87}\text{Sr}/^{86}\text{Sr}$  was assumed  
 616 to be  $0.7080 \pm 0.0005$  (2SE) for Grizzas and  $0.7050 \pm 0.0005$  (2SE) for Megas Gialos (see text). (B) Comparison  
 617 of the uncertainties expressed as % RSE (relative standard error) for unanchored mica-only ages and ages  
 618 anchored to either epidote or an assumed initial  $^{87}\text{Sr}/^{86}\text{Sr}$ . Samples from Grizzas and Megas Gialos are shown as  
 619 empty and full symbols, respectively. Location of Megas Gialos sample SYMG07 (unanchored age  $6.4 \pm 31$  Ma,  
 620 243% RSE) is shown with an arrow.

621 Model ages are also, not surprisingly, substantially more precise than unanchored mica-only  
622 Rb-Sr ages. However, their accuracy deserves scrutiny. Where epidote data are available, the  
623 model ages calculated in this work can be employed to show the effect of inaccurate initial  
624  $^{87}\text{Sr}/^{86}\text{Sr}$  in the isochron ages (**Figure 7**). At Grizzas, epidote  $^{87}\text{Sr}/^{86}\text{Sr}$  varies between 0.7043  
625 and 0.7100 (all this variation is contained in the metasomatic rind sample SYGR38). Using  
626 available bulk rock data for the Kampos Belt (**Figure 3**), this range can be extended downward  
627 to  $\sim 0.7030$ , hence effectively bracketing the possible compositions of initial Sr to calculate  
628 mica model ages. For simplicity, the same range is employed for Megas Gialos. Beyond the  
629 model ages presented in the results section and **Table 2**, for each sample two additional model  
630 ages are calculated using an initial  $^{87}\text{Sr}/^{86}\text{Sr}$  of  $0.7030 \pm 0.005$  and  $0.7100 \pm 0.005$ , respectively  
631 (**Figure 7 and Supplementary Table S5**). In the Grizzas samples, using an initial  $^{87}\text{Sr}/^{86}\text{Sr}$  of  
632 0.7100 generates model ages that are generally within uncertainty of those where the initial  
633  $^{87}\text{Sr}/^{86}\text{Sr}$  was assumed to be 0.7080; conversely, the ages are  $\geq 10\%$  older if an initial  $^{87}\text{Sr}/^{86}\text{Sr}$   
634 value of 0.7030 is employed. **Figure 7** shows that the older the sample, the more dramatic is  
635 the impact of the initial  $^{87}\text{Sr}/^{86}\text{Sr}$  chosen. For the  $> 40$  Ma Grizzas micas, the use of initial  
636  $^{87}\text{Sr}/^{86}\text{Sr}$  of 0.7100 provides ages that are resolvable (i.e. outside 2SE) from those obtained  
637 employing 0.7030 as the initial  $^{87}\text{Sr}/^{86}\text{Sr}$  ratio. Conversely, for the younger ( $< 30$  Ma) Megas  
638 Gialos samples, all the calculated model ages are within uncertainty of each other. While the  
639 favored approach remains to analyze a low Rb/Sr phase cogenetic to mica (e.g., epidote,  
640 plagioclase, carbonate, apatite), where there is limited independent knowledge of initial Sr  
641 isotope compositions, we recommend employing  $^{87}\text{Sr}/^{86}\text{Sr}$  that are intermediate between those  
642 of likely endmembers representative of the examined lithologies.

643  
644 At Grizzas, the blueschist blocks (samples SYGR36 and SYGR44) and a metasomatic rind  
645 (sample SYGR38) consistently yielded initial  $^{87}\text{Sr}/^{86}\text{Sr}$  values close to 0.708, although the latter  
646 shows scattering between 0.704 to 0.710 (**Figure 3**). In the literature, highly radiogenic values  
647 in metamafic and metasomatic rocks are common in the Kampos Belt, including for some  
648 metasedimentary rocks (**Figure 3**). On the other hand, a metagabbro (sample SYGR50) yielded  
649 an initial  $^{87}\text{Sr}/^{86}\text{Sr}$  value close to 0.705. Similarly, the metamafic greenschist (SYMG07) and  
650 veins (SYMG02 and SYMG08.3), along with additional vein and greenschist samples analyzed  
651 for bulk rock  $^{87}\text{Sr}/^{86}\text{Sr}$  only from Megas Gialos consistently yielded in-situ epidote and age-  
652 corrected TIMS whole rock  $^{87}\text{Sr}/^{86}\text{Sr}$  values of  $\sim 0.705$  (**Figure 3 and supplementary Table**  
653 **S4**). We interpret the least radiogenic values to represent the oceanic magmatic protolith (e.g.,  
654 Taylor and Lasaga, 1999) as well as veins that have equilibrated with or sourced from  
655 metamafic rocks. In contrast, the more radiogenic signature could have been introduced by pre-  
656 subduction seafloor alteration (Voigt et al., 2021), or metasomatism by highly radiogenic fluids  
657 for example derived from dehydration of metasedimentary rocks (Halama et al., 2011). The  
658 latter hypothesis is more consistent with the spatial association between metasedimentary and  
659 metasomatic rocks within the Grizzas shear zone. Our results demonstrate that for high-  
660 pressure metamafic rocks in subduction zones, the commonly assumed MORB-like  $^{87}\text{Sr}/^{86}\text{Sr}$   
661 value of 0.703 (Rösell and Zack, 2021) might not necessarily be representative of the initial Sr  
662 isotope composition.

663



664

665 **Figure 7.** Covariation plots showing the effect of assumed initial  $^{87}\text{Sr}/^{86}\text{Sr}$  on the mica Rb-Sr “model” age.  
 666 Preferred anchoring values are  $0.7080 \pm 0.0005$  for Grizzas and  $0.7050 \pm 0.0005$  for Megas Gialos (vertical  
 667 axis), which are compared to the extreme values in the range of observed bulk rock data for the Kampos Belt:  
 668  $0.7030 \pm 0.0005$  (orange) and  $0.7100 \pm 0.0005$  (green) (horizontal axis).

## 669 Application to Syros

670 To further validate our newly acquired mica Rb-Sr ages (anchored to epidote or, when not  
 671 available, to a modeled initial  $^{87}\text{Sr}/^{86}\text{Sr}$ ; **Table 2**), we compare them with published age  
 672 constraints from Kampos Belt (Top CBU) and Middle CBU localities (**Figure 8**). Kotowski et  
 673 al. (2022) and Glodny and Ring (2022) compiled and reported new ID TIMS Rb-Sr ages,  
 674 mostly from the Western Kampos Belt and outcrops along the Top CBU in Syros, ranging from  
 675 53 to 43 Ma. This age range is interpreted to date the eclogite-to-blueschist-facies subduction  
 676 fabrics, developed during the prograde-to-peak-pressure and earliest stage of exhumation.  
 677 Robust U-Pb zircon and Lu-Hf garnet ages between 53 and 48 Ma constrain the peak  
 678 metamorphism in the Grizzas area (see Tomascheck et al., 2003; Lagos et al., 2007) and are in

679 agreement with the higher end of the Rb-Sr multi-mineral isochron ages including white mica  
680 separates (e.g., Glodny and Ring 2022). Recent in-situ Rb-Sr dating of white mica also showed  
681 an age of  $48.4 \pm 3.6$  Ma for an eclogite from the Kathergaki cape (presumably belonging to the  
682 Top CBU), which was also interpreted to date the near-peak metamorphism (Barnes et al.,  
683 2024). At Grizzas, a blueschist block (SYGR36), an altered metagabbro (SYGR42) and a  
684 metasediment (SYGR45) yielded mica Rb-Sr ages varying from  $46.6 \pm 4.6$  Ma to  $47.2 \pm 3.8$   
685 Ma (**Table 2** and **Figure 6**). Similarly, the dilational vein sample SYGR41 returned a mica Rb-  
686 Sr age consistent with the HP metamorphic stage ( $44.7 \pm 4.5$  Ma). These ages overlap with the  
687 low-end of the HP eclogite-to-blueschist-facies near-peak metamorphism (peak to the earliest  
688 exhumation). Thus, and in line with previous investigations, the obtained ages are interpreted  
689 to date near-peak metamorphism (for the blueschist SYGR36 and metasediment SYGR45  
690 samples) as well as the oldest record of near-peak fluid-rock interactions and shear zone  
691 development leading to veining (SYGR41) and metagabbro fluid-assisted deformation  
692 (SYGR42).

693  
694 Kotowski et al. (2022) and Glodny and Ring (2022) noted that ages for the retrograde stage  
695 associated with early decompression in the epidote blueschist-facies are in the 45 to 40 Ma  
696 range, which could also be related to a mixed signal due to partial re-equilibration between the  
697 early lawsonite blueschist- and HP greenschist-facies metamorphism. Blueschist- to  
698 (HP)greenschist-facies retrogression during exhumation is constrained to occur between 40 and  
699 20 Ma in the Kampos Belt based on previous Rb-Sr and Ar-Ar geochronology (Glodny and  
700 Ring, 2022; Kotowski et al., 2022; Laurent et al., 2017). The metasomatic rind samples  
701 SYGR37 and SYGR38 yielded mica Rb-Sr ages more consistent with metasomatism and fluid-  
702 rock interactions during the early exhumation stage in the epidote blueschist-facies stability  
703 field ( $41.1 \pm 3.1$  Ma and  $43.0 \pm 5.4$  Ma), although sample SYGR38 could be similarly  
704 interpreted to date the metasomatism at near-peak pressure conditions considering the age  
705 uncertainty. These c. 43 and 41 Ma ages date continuous fluid-rock interaction during HP  
706 deformation, which preferentially occurs along shear zones (Zack and John, 2007; Angiboust  
707 et al., 2014; Kleine et al., 2014; Smit and Pogge von Strandmann, 2020; Rajič et al., 2024).  
708 Only one sample (felsic pod SYGR58) shows a statistically younger age of  $36.1 \pm 2.1$  Ma,  
709 which is within the period of exhumation and transition from blueschist to HP greenschist-  
710 facies. This age is consistent with petrographic evidence of chlorite pseudomorphs after garnet  
711 suggestive of selective greenschist-facies retrogression.

712  
713 Overall, our near-peak ages align with two ages (samples 9C and 27; see **Figure 8**) reported  
714 by Gyomlai et al. (2023a) for metasomatic lithologies within the Kampos Belt (Lia side), while  
715 our HP early exhumation ages are comparable, within uncertainty, to one of their ages (sample  
716 9A). Additionally, Gyomlai et al. (2023a) obtained three ages of c. 36 Ma (samples Ln57, Ln10  
717 and Ln1), overlapping with our sample SYGR58 (felsic pod), which they interpreted as  
718 retrograde ages dating the “main” metasomatic event along Kampos. Our data points to at least  
719 one event of HP metasomatism and fluid-rock interactions along the Grizzas shear zone within  
720 the range of  $46.6 \pm 4.6$  Ma to  $41.1 \pm 3.1$  Ma. Due to method uncertainties, distinguishing  
721 between multiple events within this time range is not feasible. Thus, our data suggest that fluid-  
722 rock interactions and metasomatism began under near-peak metamorphic conditions and

723 continued during the early stages of HP exhumation. These results agree with Ar-Ar ages  
724 constraining the activity of the Lia shear zone (norther boundary of the Kampos belt; see Figure  
725 1A) at near-peak to blueschist-facies exhumation conditions in the ~51 to 35 Ma range (and  
726 locally down to 23 Ma due to later greenschist-facies activity; Laurent et al., 2021).  
727 Furthermore, Barnes et al. (2024) reported an in-situ white mica Rb-Sr age of  $44.5 \pm 3.1$  Ma  
728 for a metasomatic eclogite (Delfini locality; presumably Middle CUB), suggesting that  
729 metasomatism in this section of the nappe stack also initiated at HP conditions.

730

731 This enables us to constrain localized shear zone activity under HP conditions within the  
732 subduction channel in the presence of fluids. Although previous studies have attempted to  
733 estimate the P-T conditions of formation of these metasomatic lithologies along the Kampos  
734 belt, the results vary widely, potentially suggesting that metasomatism may have occurred  
735 throughout the prograde to exhumation path (Marschall et al., 2006; Miller et al., 2009;  
736 Gyomlai et al., 2021). This is confirmed by novel reaction-path thermodynamic modelling  
737 approaches, demonstrating that bulk rock compositions, particularly the activity of elements  
738 such as Ca and Mg, play a primary role in the formation of these metasomatic rocks (Codillo  
739 et al., 2022). These metasomatic and fluid-rock interaction events may thus be temporally and  
740 spatially associated with processes such as deep slicing, underplating, and slow slip and tremor  
741 (Angiboust et al., 2012; Behr et al. 2018; Agard et al., 2018; Muñoz-Montecinos et al., 2020;  
742 Tewksbury-Christle et a., 2021; Behr and Bürgmann, 2021).

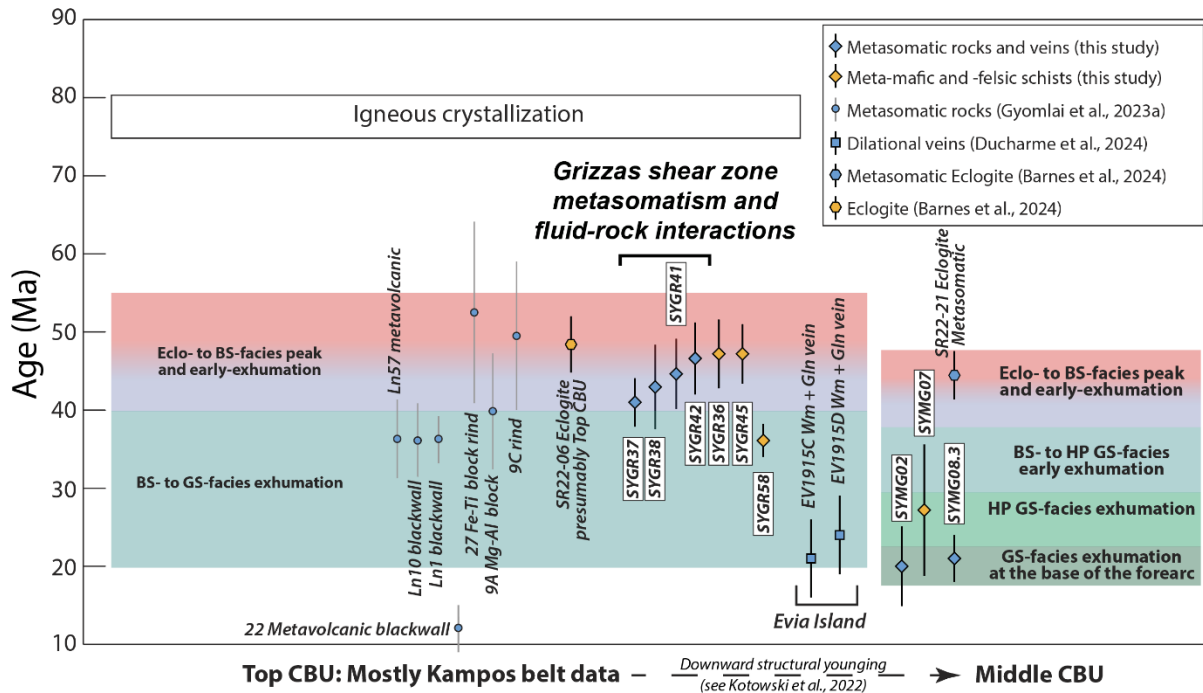
743

744 In the Megas Gialos locality, the host greenschist sample yielded an age of  $27.4 \pm 8.4$  Ma, in  
745 line with previous investigations of lithologies from the Middle CBU which have shown ages  
746 of greenschist-facies metamorphism younger than c. 35 Ma using Ar-Ar and ID TIMS Rb-Sr  
747 geochronology (Glodny and Ring, 2022; Bröcker et al., 2013). The vein samples SYMG02 and  
748 SYMG08.3 yielded potentially younger (although not statistically resolvable) ages of  $19.8 \pm$   
749  $5.2$  Ma and  $20.8 \pm 3.1$  Ma, interpreted to date dilational veining during the latest stages of  
750 exhumation of the metamorphic nappe at the base of the forearc (Cisneros et al., 2020; Muñoz-  
751 Montecinos and Behr, 2023). These ages align with phengite + glaucophane veins from the  
752 Top CBU unit (Elvia Island), which yielded virtually identical in-situ white mica Rb-Sr  
753 (anchored to glaucophane) ages for dilational veining at conditions of c. 350 °C and 0.8 GP  
754 (Ducharme et al., 2024). Thus, the finding of similar ages for transitional blueschist-to-  
755 greenschist-facies dilational veining in Syros and in Evia Island demonstrates that across-dip  
756 fluid flow toward the forearc was an ubiquitous process that occurred along the Hellenic  
757 subduction zone at c. 20-22 Ma.

758

759





760  
 761 **Figure 8.** Summary of in-situ mica Rb-Sr ages from this study along with previous investigations in Syros Island  
 762 and other localities along the CBU (Evia Island). The fields depicting the timing of the main tectonometamorphic  
 763 events represents a synthesis of the compilations from Kotowski et al. (2022) and Glodny and Ring (2022),  
 764 including white mica Rb-Sr and Ar-Ar, U-Pb in zircon and Lu-Hf in garnet, to which the reader is referred to for  
 765 a more complete compilation of the geochronologic data collected in Syros and all along the CBU. BS –  
 766 blueschist; Eclo – eclogite; GS – greenschist; HP – high pressure.

## 767 Summary

768 We systematically evaluated the limitations of mica Rb-Sr dating by LA-ICP-MS/MS for  
 769 young meta-mafic samples using metamorphic rocks from Syros and attempted to circumvent  
 770 these limitations by anchoring the initial  $^{87}\text{Sr}/^{86}\text{Sr}$  component to either a low  $^{87}\text{Rb}/^{86}\text{Sr}$  phase  
 771 (i.e. epidote) or a modeled value. White mica analysis yielded narrow  $^{87}\text{Rb}/^{86}\text{Sr}$  spread (ranging  
 772 from 14 to 231 across the whole dataset), along with unradiogenic and imprecise  $^{87}\text{Sr}/^{86}\text{Sr}$   
 773 (generally  $<0.8$ ; 2SE typically exceeding 1%). The combined effect of low  $^{87}\text{Rb}/^{86}\text{Sr}$  values,  
 774 limited spread in Rb/Sr and high uncertainty in  $^{87}\text{Sr}/^{86}\text{Sr}$  resulted in mica-only ages (i.e. without  
 775 anchoring) with very large uncertainties of 10 to 35% RSE or higher in some cases.

776  
 777 By anchoring these data to a low Rb/Sr phase such as epidote, age precision improved by up  
 778 to six times, aligning with previous Rb-Sr TIMS data from Syros and other localities along the  
 779 Cyclades blueschists unit. Such improvement is contingent to the employment of a MC-ICP-  
 780 MS instrument to obtain accurate and precise Sr isotope values for the low Rb/Sr phase by laser  
 781 ablation compared to the considerably lower precision of similar analyses by LA-ICP-MS/MS  
 782 (Barnes et al., 2024). A first set of samples yielded ages consistent with near-peak to early  
 783 exhumation along the epidote-blueschist-facies. The youngest ages likely date the latest stage  
 784 of (HP)greenschist-facies exhumation. These ages are interpreted as dating various  
 785 metasomatic stages that likely initiated at near-peak metamorphic conditions and continued

786 during exhumation. We noted unexpectedly high radiogenic  $^{87}\text{Sr}/^{86}\text{Sr}$  values and sometimes  
787 variability for the metamafic-metasomatic materials. These values, likely resulting from  
788 focused fluid flow and metasomatism along the studied shear zone, underscore the importance  
789 of carefully selecting and evaluating the geologic context of  $^{87}\text{Sr}/^{86}\text{Sr}$  anchors for future  
790 applications of this “model” Rb-Sr white mica dating methodology.

## 791 **Data availability**

792 All Laser Ablation ICP-MS/MS and MC-ICP-MS data is available in the supplementary  
793 material.

## 794 **Author contribution**

795 JM-M, AG and SV designed the study and performed the experiments, with contributions  
796 from BP. JM-M and WB collected the studied samples. AG and SO developed the statistical  
797 analysis. JM-M and AG prepared the manuscript with contributions from all co-authors.

## 798 **Competing interests**

799 The authors declare that they have no conflict of interest.

## 800 **Acknowledgments**

801 We would like to thank Madalina Jaggi and Marcel Guillong for invaluable technical support  
802 and Heather Stoll for granting access to the Agilent 8800 employed in this work. We  
803 acknowledge the constructive reviews provided by T. Gyomlai and B. Ribeiro, as well as D.  
804 Rubatto for the editorial handling of this manuscript. This project was supported by the Swiss  
805 National Foundation (Ambizione fellowship n. PZ00P2\_180126/1 to A. Giuliani) and ERC  
806 Starting Grant (947659) awarded to W.M. Behr.

807  
808  
809  
810  
811  
812  
813  
814  
815  
816

# References

- 818 1. Agard, P., Plunder, A., Angiboust, S., Bonnet, G., & Ruh, J. (2018). The subduction  
819 plate interface: Rock record and mechanical coupling (from long to short timescales).  
820 *Lithos*, 320, 537-566.
- 821 2. Angiboust, S., Wolf, S., Burov, E., Agard, P., & Yamato, P. (2012). Effect of fluid  
822 circulation on subduction interface tectonic processes: Insights from thermo-  
823 mechanical numerical modelling. *Earth and Planetary Science Letters*, 357, 238-248.
- 824 3. Angiboust, S., Pettke, T., De Hoog, J. C., Caron, B., & Oncken, O. (2014).  
825 Channelized fluid flow and eclogite-facies metasomatism along the subduction shear  
826 zone. *Journal of petrology*, 55(5), 883-916.
- 827 4. Angiboust, S., Cambeses, A., Hyppolito, T., Glodny, J., Monié, P., Calderón, M., &  
828 Juliani, C. (2018). A 100-my-long window onto mass-flow processes in the  
829 Patagonian Mesozoic subduction zone (Diego de Almagro Island, Chile). *Bulletin*,  
830 130(9-10), 1439-1456.
- 831 5. Angiboust, S., & Glodny, J. (2020). Exhumation of eclogitic ophiolitic nappes in the  
832 W. Alps: New age data and implications for crustal wedge dynamics. *Lithos*, 356,  
833 105374.
- 834 6. Barnes, C. J., Zack, T., Bukala, M., Rösel, D., Mark, C., & Schneider, D. A. (2024).  
835 Dating metamorphic processes and identifying  $^{87}\text{Sr}/^{86}\text{Sr}$  inheritance using volume-  
836 coupled Rb/Sr geochronology and geochemistry of in situ white mica: A  
837 demonstration with HP/LT rocks from Syros, Greece. *Chemical Geology*, 122149.
- 838 7. Bastias, J., Spikings, R., Riley, T., Chew, D., Grunow, A., Ulianov, A., ... & Burton-  
839 Johnson, A. (2023). Cretaceous magmatism in the Antarctic Peninsula and its tectonic  
840 implications. *Journal of the Geological Society*, 180(1), jgs2022-067.
- 841 8. Behr, W. M., Kotowski, A. J., & Ashley, K. T. (2018). Dehydration-induced  
842 rheological heterogeneity and the deep tremor source in warm subduction zones.  
843 *Geology*, 46(5), 475-478.
- 844 9. Behr, W. M., & Bürgmann, R. (2021). What's down there? The structures, materials  
845 and environment of deep-seated slow slip and tremor. *Philosophical Transactions of*  
846 *the Royal Society A*, 379(2193), 20200218.
- 847 10. v. Blanckenburg, F., Villa, I. M., Baur, H., Morteani, G., & Steiger, R. H. (1989).  
848 Time calibration of a PT-path from the Western Tauern Window, Eastern Alps: the  
849 problem of closure temperatures. *Contributions to mineralogy and Petrology*, 101(1),  
850 1-11.
- 851 11. Breeding, C. M., Ague, J. J., & Bröcker, M. (2004). Fluid–metasedimentary rock  
852 interactions in subduction-zone mélangé: implications for the chemical composition  
853 of arc magmas. *Geology*, 32(12), 1041-1044.
- 854 12. Bröcker, M., & Enders, M. (2001). Unusual bulk-rock compositions in eclogite-facies  
855 rocks from Syros and Tinos (Cyclades, Greece): implications for U–Pb zircon  
856 geochronology. *Chemical Geology*, 175(3-4), 581-603.
- 857 13. Bröcker, M., Baldwin, S., & Arkudas, R. (2013). The geological significance of  
858  $^{40}\text{Ar}/^{39}\text{Ar}$  and Rb–Sr white mica ages from Syros and Sifnos, Greece: a record of  
859 continuous (re) crystallization during exhumation?. *Journal of Metamorphic Geology*,  
860 31(6), 629-646.

- 861 14. Burg, J. P., & Bouilhol, P. (2019). Timeline of the South Tibet–Himalayan belt: The  
862 geochronological record of subduction, collision, and underthrusting from zircon and  
863 monazite U–Pb ages. *Canadian Journal of Earth Sciences*, 56(12), 1318-1332.
- 864 15. Ceccato, A., Behr, W. M., Zappone, A. S., Tavazzani, L., & Giuliani, A. (2024).  
865 Structural evolution, exhumation rates, and rheology of the European crust during  
866 Alpine collision: Constraints from the Rotondo granite—Gotthard nappe. *Tectonics*,  
867 43, e2023TC008219.
- 868 16. Chew, D. M., & Spikings, R. A. (2015). Geochronology and thermochronology using  
869 apatite: time and temperature, lower crust to surface. *Elements*, 11(3), 189-194.
- 870 17. Cisneros, M., Barnes, J. D., Behr, W. M., Kotowski, A. J., Stockli, D. F., & Soukis,  
871 K. (2020). Insights from elastic thermobarometry into exhumation of high-pressure  
872 metamorphic rocks from Syros, Greece. *Solid Earth Discussions*, 2020, 1-27.
- 873 18. Cooperdock, E. H., Raia, N. H., Barnes, J. D., Stockli, D. F., & Schwarzenbach, E. M.  
874 (2018). Tectonic origin of serpentinites on Syros, Greece: Geochemical signatures of  
875 abyssal origin preserved in a HP/LT subduction complex. *Lithos*, 296, 352-364.
- 876 19. Dalton, H., Giuliani, A., Phillips, D., Hergt, J., Maas, R., Matchan, E., ... & O'Brien,  
877 H. (2020). A comparison of geochronological methods commonly applied to  
878 kimberlites and related rocks: Three case studies from Finland. *Chemical Geology*,  
879 558, 119899.
- 880 20. Ducharme, T. A., Schneider, D. A., Grasemann, B., Bukala, M., Camacho, A.,  
881 Larson, K. P., & Soukis, K. (2024). Syn-exhumation metasomatic glaucophane-  
882 phengite-quartz veins formed at moderate pressures: exploring the control of fO<sub>2</sub> and  
883 bulk composition on nominally HP metamorphic assemblages. *Contributions to  
884 Mineralogy and Petrology*, 179(3), 1-25.
- 885 21. Fitzpayne, A., Giuliani, A., Hergt, J., Woodhead, J. D., & Maas, R. (2020). Isotopic  
886 analyses of clinopyroxenes demonstrate the effects of kimberlite melt metasomatism  
887 upon the lithospheric mantle. *Lithos*, 370, 105595.
- 888 22. Fitzpayne, A., Giuliani, A., Howarth, G. H., Peters, B. J., Fehr, M. A., & Maas, R.  
889 (2023). Major-, trace-element and Sr-Nd-Hf isotope geochemistry of diamondiferous  
890 dykes from Tonguma and Koidu, Sierra Leone: highly micaceous kimberlites formed  
891 by assimilation of metasomatised lithospheric mantle rocks. *Chemical Geology*, 630,  
892 121475.
- 893 23. Gautier, P., & Brun, J. P. (1994). Ductile crust exhumation and extensional  
894 detachments in the central Aegean (Cyclades and Evvia Islands). *Geodinamica Acta*,  
895 7(2), 57-85.
- 896 24. Giuliani, A., Oesch, S., Guillong, M., & Howarth, G. H. (2024). Mica RbSr dating by  
897 laser ablation ICP-MS/MS using an isochronous calibration material and application  
898 to West African kimberlites. *Chemical Geology*, 121982.
- 899 25. Glodny, J., Grauert, B., Fiala, J., Vejnar, Z., & Krohe, A. (1998). Metapegmatites in  
900 the western Bohemian massif: ages of crystallisation and metamorphic overprint, as  
901 constrained by U–Pb zircon, monazite, garnet, columbite and Rb–Sr muscovite data.  
902 *Geologische Rundschau*, 87, 124-134.
- 903 26. Glodny, J., Pease, V., Montero, P., Austrheim, H., & Rusin, A. I. (2004). Protolith  
904 ages of eclogites, Marun-Keu Complex, Polar Urals, Russia: implications for the pre-  
905 and early Uralian evolution of the northeastern European continental margin.  
906 *Geological Society, London, Memoirs*, 30(1), 87-105.
- 907 27. Glodny, J., Kühn, A., & Austrheim, H. (2008). Geochronology of fluid-induced  
908 eclogite and amphibolite facies metamorphic reactions in a subduction–collision  
909 system, Bergen Arcs, Norway. *Contributions to Mineralogy and Petrology*, 156, 27-  
910 48.

- 911 28. Glodny, J., & Ring, U. (2022). The Cycladic Blueschist Unit of the Hellenic  
912 subduction orogen: Protracted high-pressure metamorphism, decompression and  
913 reimbrication of a diachronous nappe stack. *Earth-Science Reviews*, 224, 103883.
- 914 29. Gou, L. L., Long, X. P., Yan, H. Y., Shu, T. C., Wang, J. Y., Xu, X. F., ... & Tian, Z.  
915 B. (2022). Metamorphic P–T Evolution and In Situ Biotite Rb–Sr Geochronology of  
916 Garnet–Staurolite Schist From the Ramba Gneiss Dome in the Northern Himalaya.  
917 *Frontiers in Earth Science*, 10, 887154.
- 918 30. Gyomlai, T., Agard, P., Jolivet, L., Larvet, T., Bonnet, G., Omrani, J., ... & Noël, J.  
919 (2022). Cimmerian metamorphism and post Mid-Cimmerian exhumation in Central  
920 Iran: Insights from in-situ Rb/Sr and U/Pb dating. *Journal of Asian Earth Sciences*,  
921 233, 105242.
- 922 31. Gyomlai, T., Agard, P., Marschall, H. R., & Jolivet, L. (2023a). Hygrochronometry of  
923 punctuated metasomatic events during exhumation of the Cycladic blueschist unit  
924 (Syros, Greece). *Terra Nova*, 35(2), 101-112.
- 925 32. Gyomlai, T., Agard, P., Herviou, C., Jolivet, L., Monié, P., Mendes, K., & Iemmolo,  
926 A. (2023b). In situ Rb–Sr and <sup>40</sup>Ar–<sup>39</sup>Ar dating of distinct mica generations in the  
927 exhumed subduction complex of the Western Alps. *Contributions to Mineralogy and  
928 Petrology*, 178(9), 58.
- 929 33. Halama, R., John, T., Herms, P., Hauff, F., & Schenk, V. (2011). A stable (Li, O) and  
930 radiogenic (Sr, Nd) isotope perspective on metasomatic processes in a subducting  
931 slab. *Chemical Geology*, 281(3-4), 151-166.
- 932 34. Halama, R., Konrad-Schmolke, M., & De Hoog, J. C. (2020). Boron isotope record of  
933 peak metamorphic ultrahigh-pressure and retrograde fluid–rock interaction in white  
934 mica (Lago di Cignana, Western Alps). *Contributions to Mineralogy and Petrology*,  
935 175(3), 20.
- 936 35. Hogmalm, K.J., Zack, T., Karlsson, A.K.O., Sjöqvist, A.S.L., Garbe-Schönberg, D.,  
937 2017. In situ Rb–Sr and K–Ca dating by LA-ICP-MS/MS: an evaluation of N<sub>2</sub>O and  
938 SF<sub>6</sub> as reaction gases. *Journal of Analytical Atomic Spectrometry* 32(2), 305-313.
- 939 36. Holtmann, R., Muñoz-Montecinos, J., Angiboust, S., Cambeses, A., Bonnet, G.,  
940 Brown, A., ... & Agard, P. (2022). Cretaceous thermal evolution of the closing Neo-  
941 Tethyan realm revealed by multi-method petrochronology. *Lithos*, 422, 106731.
- 942 37. Huang, C., Wang, H., Shi, W., Sun, J., Hu, F., Xu, L., ... & Yang, J. (2023). In situ  
943 Rb-Sr dating of mica by LA-ICP-MS/MS. *Science China Earth Sciences*, 66(11),  
944 2603-2621.
- 945 38. Hyppolito, T., Angiboust, S., Juliani, C., Glodny, J., Garcia-Casco, A., Calderón, M.,  
946 & Chopin, C. (2016). Eclogite-, amphibolite- and blueschist-facies rocks from Diego  
947 de Almagro Island (Patagonia): Episodic accretion and thermal evolution of the  
948 Chilean subduction interface during the Cretaceous. *Lithos*, 264, 422-440.
- 949 39. Jäger, E., Niggli, E., Wenk, E., 1967. Rb-Sr Altersbestimmungen an Glimmern der  
950 Zentralalpen. In: *Beiträge zur Geologischen Karte der Schweiz*. vol. 134 Kümmerly &  
951 Frey, Bern.
- 952 40. John, T., Gussone, N., Podladchikov, Y. Y., Bebout, G. E., Dohmen, R., Halama, R.,  
953 ... & Seitz, H. M. (2012). Volcanic arcs fed by rapid pulsed fluid flow through  
954 subducting slabs. *Nature Geoscience*, 5(7), 489-492.
- 955 41. Jolivet, L., Lecomte, E., Huet, B., Denèle, Y., Lacombe, O., Labrousse, L., ... & Mehl,  
956 C. (2010). The north cycladic detachment system. *Earth and Planetary Science  
957 Letters*, 289(1-2), 87-104.
- 958 42. Keay, S., 1998. The Geological Evolution of the Cyclades, Greece: Constraints from  
959 SHRIMP U-Pb Geochronology. Unpublished PhD Thesis . Australian National  
960 University , Canberra .

- 961 43. Keiter, M., Ballhaus, C., & Tomaschek, F. (2011). A new geological map of the  
962 Island of Syros (Aegean Sea, Greece): Implications for lithostratigraphy and structural  
963 history of the Cycladic Blueschist Unit (Vol. 481). Geological Society of America.  
964 44. Kirchner, K. L., Behr, W. M., Loewy, S., & Stockli, D. F. (2016). Early Miocene  
965 subduction in the western Mediterranean: Constraints from Rb-Sr multiminerall  
966 isochron geochronology. *Geochemistry, Geophysics, Geosystems*, 17(5), 1842-1860.  
967 45. Kirkland, C. L., Olierook, H. K., Danišik, M., Liebmann, J., Hollis, J., Ribeiro, B. V.,  
968 & Rankenburg, K. (2023). Dating mylonitic overprinting of ancient rocks.  
969 *Communications Earth & Environment*, 4(1), 47.  
970 46. Kleine, B. I., Skelton, A. D., Huet, B., & Pitcairn, I. K. (2014). Preservation of  
971 blueschist-facies minerals along a shear zone by coupled metasomatism and fast-  
972 flowing CO<sub>2</sub>-bearing fluids. *Journal of Petrology*, 55(10), 1905-1939.  
973 47. Kotowski, A. J., Cisneros, M., Behr, W. M., Stockli, D. F., Soukis, K., Barnes, J. D.,  
974 & Ortega-Arroyo, D. (2022). Subduction, underplating, and return flow recorded in  
975 the Cycladic Blueschist Unit exposed on Syros, Greece. *Tectonics*, 41(6),  
976 e2020TC006528.  
977 48. Kutzschbach, M., & Glodny, J. (2024). LA-ICP-MS/MS-based Rb–Sr isotope  
978 mapping for geochronology. *Journal of Analytical Atomic Spectrometry*, 39(2), 455-  
979 477.  
980 49. Lagos, M., Scherer, E. E., Tomaschek, F., Münker, C., Keiter, M., Berndt, J., &  
981 Ballhaus, C. (2007). High precision Lu–Hf geochronology of Eocene eclogite-facies  
982 rocks from Syros, Cyclades, Greece. *Chemical Geology*, 243(1-2), 16-35.  
983 50. Laurent, V., Lanari, P., Nair, I., Augier, R., Lahfid, A., & Jolivet, L. (2018).  
984 Exhumation of eclogite and blueschist (Cyclades, Greece): Pressure–temperature  
985 evolution determined by thermobarometry and garnet equilibrium modelling. *Journal*  
986 *of metamorphic geology*, 36(6), 769-798.  
987 51. Li, K., Li, G. Y., Du, Y. F., Han, W., Zhang, J., Chen, L. H., ... & Li, L. (2021).  
988 Intraslab remobilization of nitrogen during early subduction facilitates deep nitrogen  
989 recycling: Insights from the blueschists in the Heilongjiang Complex in NE China.  
990 *Chemical Geology*, 583, 120474.  
991 52. Marschall, H. R., Ludwig, T., Altherr, R., Kalt, A., & Tonarini, S. (2006). Syros  
992 metasomatic tourmaline: evidence for very high- $\delta^{11}\text{B}$  fluids in subduction zones.  
993 *Journal of Petrology*, 47(10), 1915-1942.  
994 53. . Miller, D. P., Marschall, H. R., & Schumacher, J. C. (2009). Metasomatic formation  
995 and petrology of blueschist-facies hybrid rocks from Syros (Greece): Implications for  
996 reactions at the slab–mantle interface. *Lithos*, 107(1-2), 53-67.  
997 54. Muñoz-Montecinos, J., Angiboust, S., Cambeses, A., & García-Casco, A. (2020).  
998 Multiple veining in a paleo–accretionary wedge: The metamorphic rock record of  
999 prograde dehydration and transient high pore-fluid pressures along the subduction  
1000 interface (Western Series, central Chile). *Geosphere*, 16(3), 765-786.  
1001 55. Muñoz-Montecinos, J., Angiboust, S., & Garcia-Casco, A. (2021). Blueschist-facies  
1002 paleo-earthquakes in a serpentinite channel (Zagros suture, Iran) enlighten  
1003 seismogenesis in Mariana-type subduction margins. *Earth and Planetary Science*  
1004 *Letters*, 573, 117135.  
1005 56. Muñoz-Montecinos, J., & Behr, W. M. (2023). Transient Permeability of a Deep-  
1006 Seated Subduction Interface Shear Zone. *Geophysical Research Letters*, 50(20),  
1007 e2023GL104244.  
1008 57. Olierook, H. K., Rankenburg, K., Ulrich, S., Kirkland, C. L., Evans, N., Brown, S., ...  
1009 & Darragh, M. (2020). Resolving multiple geological events using in situ Rb-Sr

- 1010 geochronology: implications for metallogensis at Tropicana, Western Australia.  
1011 Geochronology Discussions, 2020, 1-31.
- 1012 58. Paton, C., Woodhead, J. D., Hergt, J. M., Phillips, D., & Shee, S. (2007). Strontium  
1013 isotope analysis of kimberlitic groundmass perovskite via LA-MC-ICP-MS.  
1014 Geostandards and Geoanalytical Research, 31(4), 321-330.
- 1015 59. Paton, C., Hellstrom, J., Paul, B., Woodhead, J., & Hergt, J. (2011). Iolite: Freeware  
1016 for the visualisation and processing of mass spectrometric data. Journal of Analytical  
1017 Atomic Spectrometry, 26(12), 2508-2518.
- 1018 60. Phillips, D., Zhong, D., Matchan, E. L., Maas, R., Farr, H., O'Brien, H., & Giuliani,  
1019 A. (2017, September). A comparison of geochronology methods applied to  
1020 kimberlites and related rocks from the Karelian Craton, Finland. In International  
1021 Kimberlite Conference: Extended Abstracts (Vol. 11).
- 1022 61. Pimenta Silva, M., Marxer, F., Keller, T., Giuliani, A., Ulmer, P., & Müntener, O.  
1023 (2023). Alkaline magmas in shallow arc plutonic roots: a field and experimental  
1024 investigation of hydrous cumulate melting in the southern Adamello batholith.  
1025 Contributions to Mineralogy and Petrology, 178(9), 64.
- 1026 62. Plank, T. (2014). The chemical composition of subducting sediments. Elsevier.
- 1027 63. Putlitz, B., Cosca, M. A., & Schumacher, J. C. (2005). Prograde mica  $40\text{Ar}/39\text{Ar}$   
1028 growth ages recorded in high pressure rocks (Syros, Cyclades, Greece). Chemical  
1029 Geology, 214(1-2), 79-98.
- 1030 64. Redaa, A., Farkaš, J., Gilbert, S., Collins, A. S., Wade, B., Löhr, S., ... & Garbe-  
1031 Schönberg, D. (2021). Assessment of elemental fractionation and matrix effects  
1032 during in situ Rb–Sr dating of phlogopite by LA-ICP-MS/MS: implications for the  
1033 accuracy and precision of mineral ages. Journal of Analytical Atomic Spectrometry,  
1034 36(2), 322-344.
- 1035 65. Regis, D., Rubatto, D., Darling, J., Cenki-Tok, B., Zucali, M., & Engi, M. (2014).  
1036 Multiple metamorphic stages within an eclogite-facies terrane (Sesia Zone, Western  
1037 Alps) revealed by Th–U–Pb petrochronology. Journal of Petrology, 55(7), 1429-1456.
- 1038 66. Ribeiro, B. V., Finch, M. A., Cawood, P. A., Faleiros, F. M., Murphy, T. D.,  
1039 Simpson, A., ... & Barrote, V. R. (2022). From microanalysis to supercontinents:  
1040 insights from the Rio Apa Terrane into the Mesoproterozoic SW Amazonian Craton  
1041 evolution during Rodinia assembly. Journal of Metamorphic Geology, 40(4), 631-  
1042 663.
- 1043 67. Ribeiro, B. V., Kirkland, C. L., Kelsey, D. E., Reddy, S. M., Hartnady, M. I., Faleiros,  
1044 F. M., ... & Clark, C. (2023a). Time-strain evolution of shear zones from  
1045 petrographically constrained Rb–Sr muscovite analysis. Earth and Planetary Science  
1046 Letters, 602, 117969.
- 1047 68. Ribeiro, B. V., Kirkland, C. L., Finch, M. A., Faleiros, F. M., Reddy, S. M., Rickard,  
1048 W. D., & Michael, I. H. (2023b). Microstructures, geochemistry, and geochronology  
1049 of mica fish: Review and advances. Journal of Structural Geology, 104947.
- 1050 69. Rubatto, D., Regis, D., Hermann, J., Boston, K., Engi, M., Beltrando, M., &  
1051 McAlpine, S. R. (2011). Yo-yo subduction recorded by accessory minerals in the  
1052 Italian Western Alps. Nature Geoscience, 4(5), 338-342.
- 1053 70. Rubatto, D., Williams, M., Markmann, T. A., Hermann, J., & Lanari, P. (2023).  
1054 Tracing fluid infiltration into oceanic crust up to ultra-high-pressure conditions.  
1055 Contributions to Mineralogy and Petrology, 178(11), 79.
- 1056 71. Salters, V. J., & Stracke, A. (2004). Composition of the depleted mantle.  
1057 Geochemistry, Geophysics, Geosystems, 5(5).
- 1058 72. Sarkar, S., Giuliani, A., Dalton, H., Phillips, D., Ghosh, S., Misev, S., & Maas, R.  
1059 (2023). Derivation of Lamproites and Kimberlites from a Common Evolving Source

- 1060 in the Convective Mantle: the Case for Southern African ‘Transitional Kimberlites’.  
 1061 *Journal of Petrology*, 64(7), egad043.
- 1062 73. Schmidt, M. W., Vielzeuf, D., & Auzanneau, E. (2004). Melting and dissolution of  
 1063 subducting crust at high pressures: the key role of white mica. *Earth and Planetary  
 1064 Science Letters*, 228(1-2), 65-84.
- 1065 74. Seman, S., Stockli, D. F., & Soukis, K. (2017). The provenance and internal structure  
 1066 of the Cycladic Blueschist Unit revealed by detrital zircon geochronology, Western  
 1067 Cyclades, Greece. *Tectonics*, 36(7), 1407-1429.
- 1068 75. Smit, M. A., & von Strandmann, P. A. P. (2020). Deep fluid release in warm  
 1069 subduction zones from a breached slab seal. *Earth and Planetary Science Letters*, 534,  
 1070 116046.
- 1071 76. Soukis, K., & Stockli, D. F. (2013). Structural and thermochronometric evidence for  
 1072 multi-stage exhumation of southern Syros, Cycladic islands, Greece. *Tectonophysics*,  
 1073 595, 148-164.
- 1074 77. Tewksbury-Christle, C. M., Behr, W. M., & Helper, M. A. (2021). Tracking deep  
 1075 sediment underplating in a fossil subduction margin: Implications for interface  
 1076 rheology and mass and volatile recycling. *Geochemistry, Geophysics, Geosystems*,  
 1077 22(3), e2020GC009463.
- 1078 78. Tillberg, M., Drake, H., Zack, T., Kooijman, E., Whitehouse, M. J., & Åström, M. E.  
 1079 (2020). In situ Rb-Sr dating of slickenfibres in deep crystalline basement faults.  
 1080 *Scientific reports*, 10(1), 562.
- 1081 79. Tillberg, M., Drake, H., Zack, T., Hogmalm, J., Kooijman, E., & Åström, M. (2021).  
 1082 Reconstructing craton-scale tectonic events via in situ Rb-Sr geochronology of poly-  
 1083 phased vein mineralization. *Terra Nova*, 33(5), 502-510.
- 1084 80. Tomaschek, F., Kennedy, A. K., Villa, I. M., Lagos, M., & Ballhaus, C. (2003).  
 1085 Zircons from Syros, Cyclades, Greece—recrystallization and mobilization of zircon  
 1086 during high-pressure metamorphism. *Journal of Petrology*, 44(11), 1977-2002.
- 1087 81. Trotet, F., Jolivet, L., & Vidal, O. (2001). Tectono-metamorphic evolution of Syros  
 1088 and Sifnos islands (Cyclades, Greece). *Tectonophysics*, 338(2), 179-206.
- 1089 82. Rajič, K., Raimbourg, H., Gion, A. M., Lerouge, C., & Erdmann, S. (2024). Tracing  
 1090 the Scale of Fluid Flow in Subduction Zone Forearcs: Implications from Fluid-Mobile  
 1091 elements. *Chemical Geology*, 122141.
- 1092 83. Redaa, A., Farkaš, J., Hassan, A., Collins, A. S., Gilbert, S., & Löhr, S. C. (2022).  
 1093 Constraints from in-situ Rb-Sr dating on the timing of tectono-thermal events in the  
 1094 Umm Farwah shear zone and associated Cu-Au mineralisation in the Southern  
 1095 Arabian Shield, Saudi Arabia. *Journal of Asian Earth Sciences*, 224, 105037.
- 1096 84. Taylor, A. S., & Lasaga, A. C. (1999). The role of basalt weathering in the Sr isotope  
 1097 budget of the oceans. *Chemical Geology*, 161(1-3), 199-214.
- 1098 85. Zack, T., & Roesel, D. (2021, December). Towards robust in-situ Rb-Sr spot ages. In  
 1099 AGU Fall Meeting Abstracts (Vol. 2021, pp. V22A-04).
- 1100 86. Uunk, B., Brouwer, F., ter Voorde, M., & Wijbrans, J. (2018). Understanding  
 1101 phengite argon closure using single grain fusion age distributions in the Cycladic  
 1102 Blueschist Unit on Syros, Greece. *Earth and Planetary Science Letters*, 484, 192-203.
- 1103 87. Vermeesch, P. (2018). IsoplotR: A free and open toolbox for geochronology.  
 1104 *Geoscience Frontiers*, 9(5), 1479-1493.
- 1105 88. Villa, I. M. (1998). Isotopic closure. *Terra nova*, 10(1), 42-47.
- 1106 89. Villa, I. M. (2016). Diffusion in mineral geochronometers: Present and absent.  
 1107 *Chemical Geology*, 420, 1-10.



- 1108 90. Villa, I.M., De Bièvre, P., Holden, N.E., Renne, P.R., 2015. IUPAC-IUGS  
1109 recommendation on the half life of  $^{87}\text{Rb}$ . *Geochimica et Cosmochimica Acta* 164,  
1110 382-385.
- 1111 91. Voigt, M., Pearce, C. R., Baldermann, A., & Oelkers, E. H. (2018). Stable and  
1112 radiogenic strontium isotope fractionation during hydrothermal seawater-basalt  
1113 interaction. *Geochimica et Cosmochimica Acta*, 240, 131-151.
- 1114 92. Volante, S., Blereau, E., Guitreau, M., Tedeschi, M., van Schijndel, V., & Cutts, K.  
1115 (2024). Current applications using key mineral phases in igneous and metamorphic  
1116 geology: perspectives for the future. Geological Society, London, Special  
1117 Publications, 537(1), 57-121.
- 1118 93. Wang, C., Alard, O., Lai, Y. J., Foley, S. F., Liu, Y., Munnikhuis, J., & Wang, Y.  
1119 (2022). Advances in in-situ Rb-Sr dating using LA-ICP-MS/MS: applications to  
1120 igneous rocks of all ages and to the identification of unrecognized metamorphic  
1121 events. *Chemical Geology*, 610, 121073.
- 1122 94. Wawrzenitz, N., Romer, R. L., Oberhänsli, R., & Dong, S. (2006). Dating of  
1123 subduction and differential exhumation of UHP rocks from the Central Dabie  
1124 Complex (E-China): constraints from microfabrics, Rb–Sr and U–Pb isotope systems.  
1125 *Lithos*, 89(1-2), 174-201.
- 1126 95. Whitney, D. L., & Evans, B. W. (2010). Abbreviations for names of rock-forming  
1127 minerals. *American mineralogist*, 95(1), 185-187.
- 1128 96. Wirth, E. A., Sahakian, V. J., Wallace, L. M., & Melnick, D. (2022). The occurrence  
1129 and hazards of great subduction zone earthquakes. *Nature Reviews Earth &*  
1130 *Environment*, 3(2), 125-140.
- 1131 97. Zack, T., Hogmalm, K.J., 2016. Laser ablation Rb/Sr dating by online chemical  
1132 separation of Rb and Sr in an oxygen-filled reaction cell. *Chemical Geology* 437, 120-  
1133 133.
- 1134 98. Zack, T., & John, T. (2007). An evaluation of reactive fluid flow and trace element  
1135 mobility in subducting slabs. *Chemical Geology*, 239(3-4), 199-216.
- 1136 99. Zametzer, A., Kirkland, C. L., Barham, M., Hartnady, M. I., Bath, A. B., &  
1137 Rankenburg, K. (2022). Episodic alteration within a gold-bearing Archean shear zone  
1138 revealed by in situ biotite Rb–Sr dating. *Precambrian Research*, 382, 106872.
- 1139 100. Zhao, H., Zhao, X. M., Le Roux, P. J., Zhang, W., Wang, H., Xie, L. W., ... &  
1140 Yang, Y. H. (2020). Natural clinopyroxene reference materials for in situ Sr isotopic  
1141 analysis via LA-MC-ICP-MS. *Frontiers in Chemistry*, 8, 594316.
- 1142